COMPUTATIONAL THERMAL SCIENCES: AN INTERNATIONAL JOURNAL

ISSN Print: 1940-2503
ISSN Online: 1940-2554

ACCEPTED OCTOBER 25TH 2017

ROTATING UNSTEADY MULTI-PHYSICO-CHEMICAL MAGNETO-MICROPOLAR TRANSPORT IN POROUS MEDIA: *GALERKIN FINITE ELEMENT STUDY*

M. Shamshuddin[1*], O. Anwar Bég[2], Sheri. Siva Reddy[3] and A. Kadir [4]
[1*]*Department of Mathematics, Vaagdevi College of Engineering, Warangal, Telangana,* ***India****.*
[2]*Fluid Mechanics, Aeronautical and Mechanical Engineering, School of Computing, Science and Engineering, Newton Building, The Crescent, Salford, M54WT, England,* ***UK.***
[3]*Department of Mathematics, GITAM University, Hyderabad Campus, Telangana,* ***India****.*
[4]*Materials, Structures and Corrosion, Mechanical Engineering, School of Computing, Science and Engineering, Newton Building, The Crescent, Salford, M54WT, England,* ***UK.***
****Corresponding author:*** shammaths@gmail.com

ABSTRACT In this paper, a mathematical model is developed for magnetohydrodynamic (MHD), incompressible, dissipative and chemically reacting micropolar fluid flow, heat and mass transfer through a porous medium from a vertical plate with Hall current, Soret and Dufour effects. The entire system rotates with uniform angular velocity about an axis normal to the plate. Rosseland's diffusion approximation is used to describe the radiative heat flux in the energy equation. The governing partial differential equations for momentum, heat, angular momentum and species conservation are transformed into dimensionless form under the assumption of low Reynolds number with appropriate dimensionless quantities. The emerging boundary value problem is then solved numerically with a Galerkin finite element method employing the weighted residual approach. The evolution of translational velocity, micro-rotation (angular velocity), temperature and concentration are studied in detail. The influence of many multi-physical parameters in these variables is illustrated graphically. Finally, the friction factor, surface heat transfer and mass transfer rate dependency on the emerging thermo-physical parameters are also tabulated. The finite element code is benchmarked with the results reported in the literature to check the validity and accuracy under some limiting cases and an excellent agreement with published solutions is achieved. The study is relevant to rotating MHD energy generators utilizing non-Newtonian working fluids and also magnetic rheo-dynamic materials processing systems.

Keywords: *Soret effect: Dufour effect: Hall magnetohydrodynamics: Chemical reaction: Micropolar fluid: Galerkin finite element method; rotating plate; porous media; MHD energy generators.*

Nomenclature

B_o Applied magnetic field strength

C Concentration of the solute [$mol\ m^{-3}$]

C_f Skin friction coefficient

C_m Wall couple stress

C_p Specific heat at constant pressure [$J\ kg^{-1}K^{-1}$]

C_s Concentration susceptability [$mol\ m^{-3}$]

C_w Concentration of the solute at the plate [$mol\ m^{-3}$]

C_∞ Free stream concentration [$mol\ m^{-3}$]

D_m Molecular diffusivity [$m^2 s^{-1}$]

Du Dufour number

Ec Eckert number

en_e Electron charge

F Radiation-conduction parameter

g Acceleration due to gravity [$m\ s^{-1}$]

G_m Species Grashof number

G_m Species Grashof number

G_r Thermal Grashof number

$\overline{H}$ Magnetic field strength

Ho The externally applied transverse magnetic field

i The imaginary unit

J' Dimensionless micro inertia coefficient

$\vec{j}$ Current strength

K Permeability of porous medium [m^2]

K_T Thermo diffusion ratio [$m^2 s^{-1}$]

M Magnetic field parameter

m_w Concentration gradient

n Non-dimensional oscillation frequency

Nu Nusselt number

p Constant pressure

P_r Prandtl number

q_r Thermal radiative heat flux [$W\ m^{-2}$]

q_w Heat flux [$W\ m^{-2}$]

Re_x Local Reynolds number

Sc Schmidt number

Sh_x Sherwood number

Sr Soret number

T Temperature of the field in the boundary layer [K]

T_m Mean fluid temperature]

T_w Wall temperature of the fluid [K]

T_∞ Temperature of the fluid in free stream [K]

u, v Velocity component along x, y-direction [$m\ s^{-1}$]

U_r Uniform reference velocity

V_o Scale suction velocity at the Plate [$m\ s^{-1}$]

x' Axis along the plate [m]

y' Axis perpendicular to the plate [m]

w_1, w_2, w_3, w_4 arbitrary test functions

t Non-dimensional time

Greek letters

Δ Eringen coupling number

β_f Coefficient of thermal expansion [K^{-1}]

β_C Coefficient of concentration expansion [K^{-1}]

ρ Density of magneto-micropolar fluid [$kg\ m^{-3}$]

σ Electrical conductivity of the fluid [$S\ m^{-1}$]

$\overline{\sigma}$ Stefan-Boltzmann constant [$W\ m^{-2}K^{-4}$]

κ Thermal conductivity [$W\ m^{-1}K^{-1}$]

$\overline{\kappa}$ Mean absorption coefficient [m^{-1}]

ν Kinematic viscosity [$m^2 s^{-1}$]

ν_r Kinematic vortex viscosity [$m^2 s^{-1}$]

γ Homogeneous chemical reaction parameter

γ' Gyroscopic viscosity [$kg\ m\ s^{-1}$]

λ Coefficient of gyro-viscosity [$kg\ m^{-1}s^{-1}$]

μ Fluid dynamic viscosity [$Pa\ s$]

θ Dimensionless temperature

ψ Dimensionless concentration

ω' Microrotation component [$m^2\ s^{-2}$]

τ_e Electron collision time

Ω Angular velocity [$Rd\ s^{-1}$]

ε Small constant quantity

1.INTRODUCTION

Non-Newtonian flows arise in many diverse branches of engineering, applied sciences and geophysics. These fluids are characterized by shear stress-strain relationships which substantially deviate from classical Newtonian fluids i.e. the Navier-Stokes equations. Modern developments in chemical and energy systems engineering have resulted in greater emphasis on microstructural rheological fluid mechanics in which suspensions are analysed with more sophisticated non-Newtonian models. A leading development in this area was pioneered by Eringen in the 1960s and termed micro-continuum fluid mechanics. Eringen introduced simple microfluids [1] to simulate the behaviour of real industrial fluids such as propellants, polymeric suspensions etc. He later simplified this model to the micropolar fluid model [2]. Micropolar fluids successfully mimic non-Newtonian fluids containing micro-constituents such as physiological liquids, lubricants, colloidal fluids, liquid crystals, paints, polymers and gels which cannot be simulated via the classical Newtonian fluid model or even other non-Newtonian models (viscoplastic, viscoelastic etc.). The micropolar fluid model framework considers fluids consisting of rigid, randomly oriented particles suspended in viscous medium where the deformation of the particle is ignored. The theory of micropolar fluids is able to describe many complex fluids by taking into account the microscopic effects arising from the local structure and gyratory micro motions of the fluid elements. Comprehensive reviews of micropolar hydrodynamics and applications can be found in the articles of Ariman *et al*. [3, 4] and the book by Lukaszewicz [5]. Micropolar fluids have been studied in many contexts including tribology [6], microbial nano-fuel cells [7], micro-machining processes [8], hemodynamics [9] and energy system thermodynamic optimization [10].

In many physico-chemical heat and mass transfer studies, related to both Newtonian and non-Newtonian fluids, thermo-diffusion (Soret) and diffuso-thermo (Dufour) effects play a prominent role. These effects are often of smaller order of magnitude in comparison with the diffusive effects associated with thermal conduction (Fourier's law) and mass diffusion (Fick's laws) and are frequently neglected. However these so-called cross diffusion effects become important if not dominant, in materials processing operations e.g. dendritic growth [11, 12], magnetic separation of colloids [13], MHD power generators [14] and aerospace combustion and flame dynamics [15, 16] where they arise in binary gas and supercritical fuel injection systems. Generally when

heat and mass transfer effects occur simultaneously in a moving fluid, the relationship between the fluxes and the driven potentials become significant. An energy flux can be generated not only by temperature gradient but also by composition gradient as well. The energy caused by a composition gradient is called the *Dufour effect* or *diffusion-thermo* effect. The energy caused by a temperature gradient is called the *Soret* effect or *thermo-diffusion* effect. The thermal Soret effect can for example also generate a very strong coupling force between the species (solute) and heat transport. Due to the significance importance of Soret and Dufour diffusion phenomena for fluids with medium molecular weight as well as very light molecular weights, in recent years substantial interest has emerged in simulation of these effects in many multi-physical transport problems. Postelnicu [17] considered magnetic free convection in porous media with Soret and Dufour effects. Alam and Rahman [18] investigated combined Dufour and Soret effects on hydromagnetic natural convection flow in a porous medium. Further studies of Newtonian flows with Soret/Dufour effects include Vasu *et al.* [19] (for wall mass flux effects), Bég *et al.* [20] (for hydromagnetic flow from an extending sheet in porous media) and Partha *et al*. [21] (for non-Darcian thermal convection). Non-Newtonian heat and mass transfer with Soret and/or Dufour effects has also attracted some attention. Bég *et al.* [22] used a finite element method to simulate two-dimensional micropolar boundary layer flows in Darcy-Forchheimer permeable materials with Soret and Dufour cross diffusion effects. Other representative studies include Bég *et al.* [23] and Kundu *et al*. [24] (again both for micropolar fluids) and Ashraf *et al.* [25] (for Maxwell viscoelastic fluids).

Magnetohydrodynamics (MHD) involves the simulation of flows in which electrically-conducting liquids or gases interact with an applied magnetic field. MHD is exploited in numerous modern industrial processes including vortex control [26], ionized propulsion systems, nuclear heat transfer control, medical treatment and energy generators. These systems are increasingly deploying or already feature more complex working fluids containing suspensions. *Magneto-micropolar flows* are therefore greatly relevant to such systems. Many investigators have examined boundary value problems (BVPs) of such fluids in recent years using a range of computational solvers. These include Kim [27], Borrelli *et al.* [28], Rawat et al. [29] who used finite elements, Zueco *et al*.[30] who employed network simulation, Bég *et al.* [31] who used finite difference methods, Vafeas *et al.* [32] who used boundary element methods and Bég *et al.* [33] who employed homotopy methods.

In the above investigations, the effect of Hall current in hydromagnetics has been excluded. However Hall currents characterize stronger magnetic field effects and generate cross-flows which are important in MHD energy generators and certain materials synthesis operations. Rotating flows in the presence of Hall currents are also of interest. Cowling [34] has shown that when the strength of the applied magnetic field is sufficiently large, Ohm's law needs to be modified to include Hall current. However, to study the effects of strong magnetic fields on the electrically conducting fluid flow, we see that the influence of the electromagnetic force is noticeable and causes anisotropic electrical conductivity in the plasma. This anisotropy in the electrical conductivity of the plasma produces a current known as the Hall current. Takhar *et al.* [35] used a finite difference scheme to obtain numerical solutions for Hall magnetohydrodynamic flow from a rotating plate. Further studies include Ghosh *et al.* [36] who also considered magnetic induction effects and Seth *et al.* [37] who considered transient and ramped wall temperature effects. These studies verified the strong influence of Hall current on both flow and heat transfer.

In the present investigation we generalize and extend existing studies [38, 39] to consider the *combined effects of Hall current, Soret and Dufour cross diffusion, first order chemical reaction and viscous dissipation on radiative magnetohydrodynamic micropolar flow, heat and mass transfer from a rotating vertical plate adjacent to a porous medium*. The non-dimensional conservation equations are solved with a Galerkin finite element method. The effect of various physical parameters on the translational velocity, micro-rotation velocity, temperature and concentration profiles as well as on local skin friction coefficient, wall couple stress, Sherwood number and Nusselt number are tabulated. Validation of the analysis has been performed by comparing the present results with those of Kundu *et al.* [24]. The current study is relevant to *high temperature* electromagnetic rheological flows in energy generators and magneto-rheological materials fabrication systems (where thermal radiation heat transfer is also significant) and has not appeared in the technical literature thus far.

2.MATHEMATICAL FORMULATION

Consider the unsteady free convection flow of an incompressible and electrically-conducting micropolar fluid, heat and mass transfer from an infinite vertical moving porous plate suspended in a homogenous, isotropic, porous medium. The physical configuration is illustrated in **Fig. 1**. Darcy's law is assumed and low Reynolds number flow (viscous-dominated). The vertical plate is assumed to be subjected to a constant heat flux, q_w and a constant concentration gradient, m_w. A magnetic field of uniform strength H_0 is applied in a direction parallel to the z' axis which is perpendicular to the flow direction. It is assumed that the induced magnetic field is negligible in comparison to the applied magnetic field. Magnetic Reynolds number is very small. Applied or polarized voltage is neglected so that no energy is added or extracted from the fluid by electrical means. The fluid is considered to be a gray, absorbing-emitting but non scattering medium and the Rosseland approximation is used to describe the radiative heat flux. The radiative heat flux in the x' direction is considered negligible in comparison with that of z' direction. Heat generation and viscous dissipation is present as are Soret and Dufour effects. Ohmic (Joule) dissipation is ignored. The magnetic micropolar fluid contains a species which is reactive and obeys first order chemical reaction. Initially, the fluid as well as plate is at rest but for time $t' > 0$, the whole system is allowed to rotate with constant velocity, Ω, in the micropolar-fluid saturated porous medium about the z' axis. The plate velocity u' oscillates in time t' with frequency n' which is given by $u' = U_r\left(1 + \varepsilon \cos n' t'\right)$. It is assumed that the plate is infinite in extent and hence all physical quantities depend only on z' and t'; that is $\partial u'/\partial x' = \partial u'/\partial y' = \partial v'/\partial x' = \partial v'/\partial y' = 0$ and so forth. When strength of magnetic field is very large, the generalized Ohm's law in absence of electric field takes the following form:

$$\vec{J} + \frac{\omega_e \tau_e}{B_0}\,\vec{J} \times \vec{H} = \sigma\left(\mu_e\,\vec{V} \times \vec{H} + \frac{1}{en_e}\nabla P_e\right) \tag{1}$$

Under the assumption that electron pressure (for weakly ionized fluid), the thermo-electric pressure and non-slip conditions are negligible, the above equation reduces to:

$$j_X = \frac{\sigma \mu_e H_0}{1+m^2}\left(mv' - u'\right) \quad and \quad j_Z = \frac{\sigma \mu_e H_0}{1+m^2}\left(mu' + v'\right) \tag{2}$$

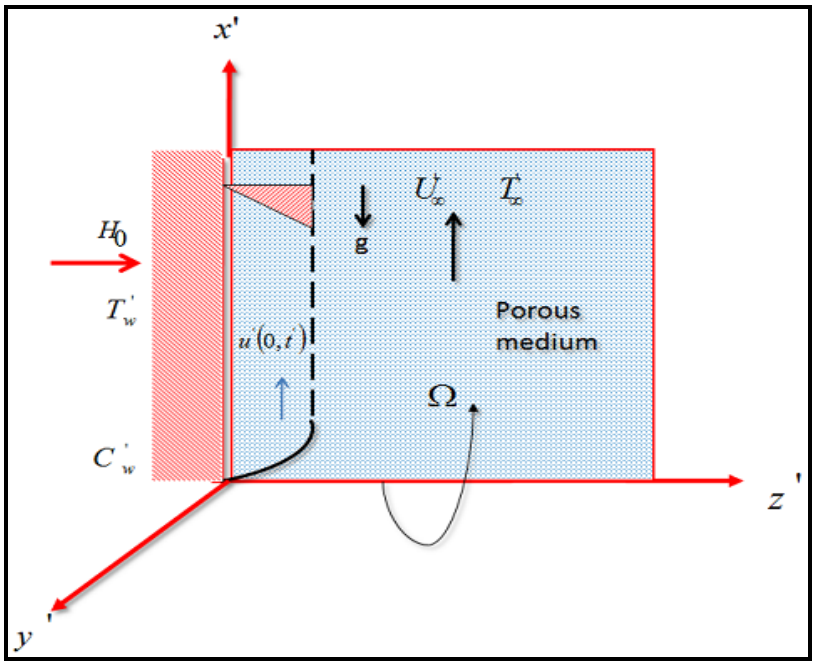

Figure .1: Flow configuration and coordinate system

Where u' is x'-component of $\vec{V}$ v' is y' component of $\vec{V}$ and $m(=\omega_e\tau_e)$ is Hall parameter. The micro-elements in micropolar fluids are of dumbbell shaped and may sustain both rotary and translation motions, as elucidated by Eringen [2, 40] and more recently by Bég *et al.* [41]. Generally each micro-element of micropolar fluid possesses six degrees of freedom (three corresponding to translation and three corresponding to rotation). Micropolar fluids can therefore support couple stresses, force stresses and may possess rotational micro-inertia of particles. The general case is however greatly simplified for two-dimensional flows, as considered here. With these foregoing assumptions, the governing equations under Boussinesq approximation can be written in a Cartesian of reference as follows:

$$\frac{\partial w'}{\partial z'} = 0 \tag{3}$$

$$\frac{\partial u'}{\partial t'} + w'\frac{\partial u'}{\partial z'} - 2\Omega v' = (\nu + \nu_r)\frac{\partial^2 u'}{\partial z'^2} + g\beta_T\left(T_w' - T_\infty'\right) + g\beta_C\left(C_w' - C_\infty'\right) - \frac{\nu\, u'}{k} - \nu_r\frac{\partial \overline{\omega}_2'}{\partial z'} + \frac{\sigma\mu_e^2 H_0^2}{\rho\left(1+m^2\right)}\left(mv' - u'\right) \tag{4}$$

$$\frac{\partial v'}{\partial t'}+w'\frac{\partial v'}{\partial z'}+2\Omega u'=(\nu+\nu_r)\frac{\partial^2 v'}{\partial z'^2}-\frac{\nu\, v'}{k}+\nu_r\frac{\partial \overline{\omega}_1'}{\partial z'}-\frac{\sigma\mu_e^2 H_0^2}{\rho\left(1+m^2\right)}\left(mu'+v'\right) \tag{5}$$

$$\rho\, j'\left(\frac{\partial \overline{\omega}_1'}{\partial t'}+w'\frac{\partial \overline{\omega}_1'}{\partial z'}\right)=\gamma'\frac{\partial^2 \overline{\omega}_1'}{\partial z'^2} \tag{6}$$

$$\rho\, j'\left(\frac{\partial \overline{\omega}_2'}{\partial t'}+w'\frac{\partial \overline{\omega}_2'}{\partial z'}\right)=\gamma'\frac{\partial^2 \overline{\omega}_2'}{\partial z'^2} \tag{7}$$

$$\frac{\partial T}{\partial t'}+w\frac{\partial T}{\partial z'}=\frac{\kappa}{\rho C_p}\left(\frac{\partial^2 T}{\partial z'^2}\right)-\frac{1}{\rho C_p}\left(\frac{\partial q_r}{\partial z'}\right)-\frac{Q'}{\rho C_p}\left(T'_w-T'_\infty\right)+\frac{\mu}{\rho C_p}\left(\frac{\partial u'}{\partial z'}\right)^2+\frac{D_m\, K_T}{cs\; cp}\frac{\partial^2 C}{\partial z'^2} \tag{8}$$

$$\frac{\partial C}{\partial t'}+w'\frac{\partial C}{\partial z'}=D_m\left(\frac{\partial^2 C}{\partial z'^2}\right)+\frac{D_m K_t}{T_m}\left(\frac{\partial^2 T}{\partial z'^2}\right)-K'_r\left(C'_w-C'_\infty\right) \tag{9}$$

The following spatial and temporal boundary conditions are prescribed:

$$\left.\begin{array}{l}\left\{t'\le 0:\ u'=v'=0\quad \overline{\omega}_1'=\overline{\omega}_2'=0\quad T=T'_\infty\,, C=C'_\infty\right.\\ \left\{t'>0: u'=U_r\left[1+\frac{\varepsilon}{2}\left(e^{in't'}+e^{-in't'}\right)\right], v'=0\,,\ \overline{\omega}_1'=\frac{-1}{2}\frac{\partial v}{\partial z'}\,, \overline{\omega}_2'=\frac{1}{2}\frac{\partial u}{\partial z'}\right.\\ \qquad (T')_{z'=0}=-\frac{q_w}{\kappa}\,,\ \ (C')_{z'=0}=-\frac{m_w}{D_m}\qquad\qquad at\quad z'=0\\ \qquad\quad and\\ \qquad\quad u'=v'=0\quad \overline{\omega}_1'=\overline{\omega}_2'=0,\ T=T'_\infty, C=C'_\infty\quad as\ z'\to\infty\end{array}\right\} \tag{10}$$

Here U_r is the uniform reference velocity and ε is a small quantity. The oscillatory plate velocity assumed in Eq. (10) is based on the model proposed by Ganapathy [42]. Integrating the mass conservation (continuity) equation (3) for *variable suction velocity normal to the plate* we consider a convenient solution to be:

$$w'=-w_0 \tag{11}$$

Where w_0 is the normal velocity at the plate $w_0>0$ for suction, $w_0<0$ for blowing. Following Rosseland's approximation (Brewster [43]), the radiative heat flux term is given by

$$q_r=\frac{-4\overline{\sigma}}{3\overline{k}}\left(\frac{\partial T^4}{\partial z'}\right) \tag{12}$$

Here $\overline{\sigma}$ is Stefan Boltzmann constant and $\overline{\kappa}$ is mean absorption coefficient. Assuming that the difference in the temperature with in the flow such that T'^4 can be expressed as a linear

combination of the temperature, using Taylor's series expansion about T'_∞, the expansion of T'^4 can be written as follows:

$$T'^4 = T'^4_\infty + 4T'^3_\infty\left(T' - T'_\infty\right) + 6T'^2_\infty\left(T' - T'_\infty\right)^2 + \ldots \tag{13}$$

Neglecting higher order terms beyond the first degree in $\left(T' - T'_\infty\right)$, we have:

$$T'^4 \cong 4T'^3_\infty T - 3T'^4_\infty \tag{14}$$

Now differentiating (12) w.r.t z' using (13) and (14), we get:

$$\frac{\partial q_r}{\partial z'} = -\left(\frac{16T^3_\infty \bar{\sigma}}{3\bar{k}}\right)\frac{\partial^2 T}{\partial z'^2} \tag{15}$$

We note that the Rosseland model is quite accurate for optically-thick media where thermal radiation propagates a limited distance prior to encountering scattering or absorption. The refractive index of the fluid-particle suspension is assumed to be constant, intensity within the fluid is nearly isotropic and uniform and wavelength regions exist where the optical thickness is usually in excess of five [44]. Introducing the following non-dimensional variables:

$$z' = \frac{\eta U_r}{\nu}, \quad u' = \frac{u}{U_r}, \; v' = \frac{v}{U_r}, \quad t' = \frac{tU_r^2}{\nu}, \quad n' = \frac{n\nu}{U_r^2}, \Delta = \frac{K}{\rho\nu}$$

$$\bar{\omega}'_1 = \frac{\bar{\omega}_1\nu}{U_r^2}, \; \bar{\omega}'_2 = \frac{\bar{\omega}_2\nu}{U_r^2}, \theta = \frac{\left(T - T_\infty\right)\kappa}{q_W}, \; \psi = \frac{\left(C - C_\infty\right)D_m}{m_W}, \tag{16}$$

Where all quantities with a prime are dimensionless, θ is dimensionless temperature function, ψ is dimensionless concentration and Δ is the Eringen micropolar vortex viscosity parameter. Substituting equation (16) into equations (2)-(7) and dropping primes yields the following dimensionless equations:

$$\frac{\partial u}{\partial t} - S\frac{\partial u}{\partial \eta} - Rv = \left(1+\Delta\right)\frac{\partial^2 u}{\partial \eta^2} + Gr\theta + Gm\psi - \left(\frac{M^2}{1+m^2} + \frac{1}{K}\right)u - \Delta\frac{\partial \bar{\omega}_2}{\partial \eta} + \left(\frac{mM^2}{1+m^2}\right)v \tag{17}$$

$$\frac{\partial v}{\partial t} - S\frac{\partial v}{\partial \eta} + Ru = \left(1+\Delta\right)\frac{\partial^2 v}{\partial \eta^2} - \left(\frac{M^2}{1+m^2} + \frac{1}{K}\right)v + \Delta\frac{\partial \bar{\omega}_1}{\partial \eta} + \left(\frac{mM^2}{1+m^2}\right)u \tag{18}$$

$$\frac{\partial \bar{\omega}_1}{\partial t} - S\frac{\partial \bar{\omega}_1}{\partial \eta} = \lambda\frac{\partial^2 \bar{\omega}_1}{\partial \eta^2} \tag{19}$$

$$\frac{\partial \overline{\omega}_2}{\partial t} - S\frac{\partial \overline{\omega}_2}{\partial \eta} = \lambda \frac{\partial^2 \overline{\omega}_2}{\partial \eta^2} \tag{20}$$

$$\frac{\partial \theta}{\partial t} - S\frac{\partial \theta}{\partial \eta} = \frac{1}{\Pr}\left(1+\frac{4F}{3}\right)\frac{\partial^2 \theta}{\partial \eta^2} - \frac{Q_H}{\Pr}\theta + + Ec\left(\frac{\partial u}{\partial \eta}\right)^2 + Du\left(\frac{\partial^2 \psi}{\partial \eta^2}\right) \tag{21}$$

$$\frac{\partial \psi}{\partial t} - S\frac{\partial \psi}{\partial \eta} = \frac{1}{Sc}\left(\frac{\partial^2 \psi}{\partial \eta^2}\right) + Sr\left(\frac{\partial^2 \theta}{\partial \eta^2}\right) - \gamma\,\psi \tag{22}$$

Here eqns. (17) and (18) are the *primary* and *secondary* translational momentum equations. Also $R = \frac{2\Omega\nu}{U_r^2}$ is the rotational parameter, $M = \frac{\mu_e H_0}{U_r}\sqrt{\frac{\sigma\nu}{\rho}}$ is the magnetic field parameter, $\Pr = \frac{\mu\rho C_p}{k}$, $Sc = \frac{\nu}{D_m}$, $Gr = \frac{\nu\, g\, \beta_T\left(T'_w - T'_\infty\right)}{U_r^3}$, and $Gm = \frac{\nu\, g\, \beta_C\left(C'_w - C'_\infty\right)}{U_r^3}$ are Prandtl number, Schmidt number, thermal Grashof and species Grashof number, respectively. $F = \frac{4T_\infty^3\overline{\sigma}}{k\overline{k}}$ is thermal radiation-conduction parameter, $K = \frac{\kappa U_r^2}{\nu^2}$ is the permeability of the porous medium, $Q' = \frac{Q_H\,\nu^2}{U_r^2\kappa}$ is heat absorption parameter, $Ec = \frac{u_o^{\,2}}{C_p(T'_w - T'_\infty)}$ is the Eckert number, $D_u = \frac{\kappa^2 K_T m_w}{q_w \rho c \mu}$ is the Dufour number, $Sr = \frac{D_m K_T\, q_w}{\kappa\, m_w}$ is the Soret number, $\gamma = \frac{K'_r\nu}{U_r}$ is chemical reaction parameter, $S = \frac{w_0}{U_r}$ is the suction parameter, $\lambda = \frac{\gamma'}{\mu j}$ is the dimensionless gyro-viscosity micropolar material parameter and $\Delta = \frac{K}{\rho\nu}$ is the Eringen coupling number (vortex viscosity ratio parameter. The boundary conditions can be written in non-dimensional form as follows:

$$\left.\begin{array}{l} \left\{ for\ t \le 0: \quad u = v = 0 \quad \overline{\omega}_1 = \overline{\omega}_2 = 0 \quad \theta = 0, \psi = 0 \right. \\ \left\{ \begin{array}{ll} for\ t > 0: & u = \left[1 + \frac{\varepsilon}{2}\left(e^{\text{int}} + e^{-\text{int}}\right)\right], v = 0\,,\ \overline{\omega}_1 = \frac{-1}{2}\frac{\partial v}{\partial \eta}\,,\ \overline{\omega}_2 = \frac{1}{2}\frac{\partial u}{\partial \eta} \\ & \theta' = -1,\ \psi' = -1 \quad at\ \ \eta = 0 \quad\ and \\ & u = v = 0 \quad \overline{\omega}_1 = \overline{\omega}_2 = 0 \quad \theta = \psi = 0 \qquad as\ \eta \to \infty \end{array} \right. \end{array}\right\} \tag{23}$$

To obtain desired solutions, we now simplify Eqns. (16) - (21) by formulating the translational velocity and angular velocity in complex form:

$$U = u + i\,v,\;\; \omega = \overline{\omega}_1 + i\,\overline{\omega}_2$$

The emerging unsteady partial differential conservation equations for linear momentum, angular momentum, energy and species conservation then assume the form:

$$\frac{\partial U}{\partial t} - S\frac{\partial U}{\partial \eta} + iRU = (1+\Delta)\frac{\partial^2 U}{\partial \eta^2} + Gr\theta + Gm\psi + i\Delta\frac{\partial \omega}{\partial \eta} - \left(\frac{M^2}{1+m^2} + \frac{1}{K}\right)U - i\left(\frac{mM^2}{1+m^2}\right)U \tag{24}$$

$$\frac{\partial \omega}{\partial t} - S\frac{\partial \omega}{\partial \eta} = \lambda\frac{\partial^2 \omega}{\partial \eta^2} \tag{25}$$

$$\frac{\partial \theta}{\partial t} - S\frac{\partial \theta}{\partial \eta} = \frac{1}{\Pr}\left(1+\frac{4F}{3}\right)\frac{\partial^2 \theta}{\partial \eta^2} - \frac{Q_H\theta}{\Pr} + Ec\left(\frac{\partial u}{\partial \eta}\right)^2 + D_u\frac{\partial^2 \psi}{\partial \eta^2} \tag{26}$$

$$\frac{\partial \psi}{\partial t} - S\frac{\partial \psi}{\partial \eta} = \frac{1}{Sc}\frac{\partial^2 \psi}{\partial \eta^2} + Sr\left(\frac{\partial^2 \theta}{\partial \eta^2}\right) - \gamma\,\psi \tag{27}$$

The associated boundary conditions (22) become:

$$\left\{\begin{array}{llll} for\ t \le 0 & U = 0, & \omega = 0, \quad \theta = 0, & \psi = 0 \\ for\ t > 0 & U = \left[1 + \frac{\varepsilon}{2}\left(e^{\mathrm{int}} + e^{-\mathrm{int}}\right)\right], & \omega = \frac{i}{2}\frac{\partial U}{\partial \eta}, \;\; \theta' = -1, \;\; \psi' = -1, & at\ \eta = 0 \\ & U = 0, \;\; \omega = 0, \quad \theta = 0, \quad \psi = 0, & as\ \ \eta \to \infty & \end{array}\right\} \tag{28}$$

3. FINITE ELEMENT SOLUTIONS

The set of time-dependent, reduced, non-dimensional, coupled partial differential equations (24)-(27) subject to boundary conditions (28) are nonlinear, coupled and therefore cannot be solved analytically. The finite element method is a powerful technique for solving ordinary differential or partial differential equations as well as integral equations. It is equally versatile at solving Newtonian and non-Newtonian problems. The variational form is particularly popular for fluid mechanics simulations and general details of this methodology are available in many textbooks. Some recent examples of applications with associated computational details of finite element modelling of *non-Newtonian magnetohydrodynamic flows* include pulsating magneto-rheo-hydrodynamics of Nakamura-Sawada bi-viscosity fluids [45], rotating extending sheet power-law nanofluid dynamics [46], radiating magneto-micropolar shrinking sheet flow in porous media [47] and dissipative second order viscoelastic nanofluid extrusion flows [48]. The fundamental steps involved in the finite-element analysis of a problem are as follows:

Step 1: *Discretization of the infinite fluid domain into finite elements:*

The whole domain is divided into a finite number of sub domains, processes known as discretization of the domain. Each sub domain is termed as finite element. The collection of elements is then denoted the finite-element mesh.

Step 2: *Derivation of element equations:*

The derivation of finite element equations *i.e.*, algebraic equations among the unknown parameters of the finite element approximation, involves the following three stages.

1. Construct the variational formulation of the differential equation.
2. Assume the form of the approximate solution over a typical finite element.
3. Derive the finite element equations by substituting the approximate solution into variational formulation.

These steps results in a matrix equation of the form $\left[K^e\right]\left\{u^e\right\}=\left\{F^e\right\}$, which defines the finite element model of the original equation.

Step 3: *Assembly of Element Equations:*

The algebraic equations so obtained are assembled by imposing the inter-element continuity conditions (i.e. the values of the nodal variables at the nodes are identical for two or more elements). This yields a large number of algebraic equations known as the *global finite element model*. This governs the whole flow domain.

Step 4: *Imposition of boundary conditions:*

The initial and final boundary conditions defined in equation (28) are imposed on the above obtained assembled equations.

Step 5: *Solution of assembled equations:*

The final matrix equation obtained can be solved by a direct or iterative method.

Variational formulation

The variational formulation associated with Eqs. (24) - (27) over a typical two-node linear element $\left(y_e,\ y_{e+1}\right)$ is given by

$$\int_{y_e}^{y_{e+1}} w_1\left[\frac{\partial U}{\partial t}-S\left(\frac{\partial U}{\partial \eta}\right)-A_2\left(\frac{\partial^2 U}{\partial \eta^2}\right)-(Gr\theta+Gm\psi)-A_3\left(\frac{\partial \omega}{\partial \eta}\right)+\left(A_1+A_4+A_5\right)U\right]d\eta=0 \qquad (29)$$

$$\int_{y_e}^{y_{e+1}} w_2\left[\frac{\partial \omega}{\partial t}-S\left(\frac{\partial \omega}{\partial \eta}\right)-\lambda\left(\frac{\partial^2 \omega}{\partial \eta^2}\right)\right]d\eta=0 \qquad (30)$$

$$\int_{y_e}^{y_{e+1}} w_3\left[\frac{\partial \theta}{\partial t}-S\left(\frac{\partial \theta}{\partial \eta}\right)-A_6\left(\frac{\partial^2 \theta}{\partial \eta^2}\right)+A_7\ \theta-Ec\left(\frac{\partial U}{\partial \eta}\right)^2-Du\frac{\partial^2 C}{\partial \eta^2}\right]d\eta=0 \qquad (31)$$

$$\int_{y_e}^{y_{e+1}} w_4\left[\frac{\partial \psi}{\partial t}-S\left(\frac{\partial \psi}{\partial \eta}\right)-\frac{1}{Sc}\left(\frac{\partial^2 \psi}{\partial \eta^2}\right)+\gamma\ \psi-Sr\frac{\partial^2 \theta}{\partial \eta^2}\right]d\eta=0 \qquad (32)$$

Where w_1, w_2, w_3 and w_4 are arbitrary test functions and may be viewed as the variations in U ω , θ and ψ respectively, and $A_1=iR$, $A_2=1+\Delta$, $A_3=i\,\Delta$, $A_4=\left(\frac{M^2}{1+m^2}+\frac{1}{K}\right)$, $A_5=i\left(\frac{mM^2}{1+m^2}\right)$, $A_6=\frac{1}{\Pr}\left(1+\frac{4F}{3}\right)$, $A_7=\left(\frac{Q_H}{\Pr}\right)$. After dropping the order of integration and non-linearity, we arrive at the following system of equations.

$$\int_{y_e}^{y_{e+1}}\left[\begin{array}{l} w_1\frac{\partial U}{\partial t}-Sw_1\left(\frac{\partial U}{\partial \eta}\right)+A_2\left(\frac{\partial w_1}{\partial \eta}\right)\left(\frac{\partial U}{\partial \eta}\right)-(Gr\ w_1\theta+Gmw_1\psi) \\ -A_3w_1\frac{\partial \omega}{\partial \eta}+w_1\left(A_1+A_4+A_5\right)U \end{array}\right]d\eta-\left[w_1\left(\frac{\partial U}{\partial \eta}\right)\right]_{y_e}^{y_{e+1}}=0 \qquad (33)$$

$$\int_{y_e}^{y_{e+1}}\left[w_2\frac{\partial \omega}{\partial t}-Sw_2\left(\frac{\partial \omega}{\partial \eta}\right)-\lambda\left(\frac{\partial w_2}{\partial \eta}\right)\left(\frac{\partial \omega}{\partial \eta}\right)\right]d\eta-\left[w_2\left(\frac{\partial \omega}{\partial \eta}\right)\right]_{y_e}^{y_{e+1}}=0 \qquad (34)$$

$$\int_{y_e}^{y_{e+1}}\left[\begin{array}{l} w_3\frac{\partial \theta}{\partial t}-Sw_3\left(\frac{\partial \theta}{\partial \eta}\right)+A_6\left(\frac{\partial w_3}{\partial \eta}\right)\left(\frac{\partial \theta}{\partial \eta}\right)+A_7w_3\theta \\ -Ec\ w_3\left(\frac{\partial \overline{U}}{\partial \eta}\right)\left(\frac{\partial U}{\partial \eta}\right)-Duw_3\left(\frac{\partial w_3}{\partial \eta}\right)\left(\frac{\partial \psi}{\partial \eta}\right) \end{array}\right]d\eta-\left[w_3\left(\frac{\partial \theta}{\partial \eta}\right)+Duw_3\frac{\partial \psi}{\partial \eta}\right]_{y_e}^{y_{e+1}}=0 \qquad (35)$$

$$\int_{y_e}^{y_{e+1}} \begin{bmatrix} w_4 \dfrac{\partial \psi}{\partial t} - Sw_4\left(\dfrac{\partial \psi}{\partial \eta}\right) + \dfrac{1}{Sc}\left(\dfrac{\partial w_4}{\partial \eta}\right)\left(\dfrac{\partial \psi}{\partial \eta}\right) + Krw_4\psi \\ Sr\left(\dfrac{\partial w_4}{\partial \eta}\right)\left(\dfrac{\partial \theta}{\partial \eta}\right) \end{bmatrix} d\eta - \left[\frac{w_4}{Sc}\left(\frac{\partial \psi}{\partial \eta}\right) + Srw_4\frac{\partial \theta}{\partial \eta}\right]_{y_e}^{y_{e+1}} = 0 \qquad (36)$$

Finite Element formulation

The finite element model may be obtained from Eqs. (33) - (36) by substituting finite element approximations of the form:

$$U = \sum_{j=1}^{2} U_j^e \chi_j^e,\ \omega = \sum_{j=1}^{2} \omega_j^e \chi_j^e,\ \theta = \sum_{j=1}^{2} \theta_j^e \chi_j^e \ and\ \psi = \sum_{j=1}^{2} \psi_j^e \chi_j^e \qquad (37)$$

With $w_1 = w_2 = w_3 = w_4 = \chi_j^e\ (i = 1, 2)$, where U_j^e, $\omega_j^e, \theta_j^e\ and\ \psi_j^e$ are the velocity in the direction of *x*-axis, *y*-axis and temperature respectively at the j^{th} node of typical e^{th} element (y_e, y_{e+1}) and χ_i^e are the shape functions for this element (y_e, y_{e+1}) and are taken as:

$$\chi_1^e = \frac{y_{e+1} - y}{y_{e+1} - y_e} and\ \chi_2^e = \frac{y - y_e}{y_{e+1} - y_e},\ y_e \le y \le y_{e+1} \qquad (38)$$

The finite element model of the equations for e^{th} element thus formed is given by.

$$\begin{bmatrix} [K^{11}] & [K^{12}] & [K^{13}] & [K^{14}] \\ [K^{21}] & [K^{22}] & [K^{23}] & [K^{24}] \\ [K^{31}] & [K^{32}] & [K^{33}] & [K^{34}] \\ [K^{41}] & [K^{42}] & [K^{43}] & [K^{44}] \end{bmatrix} \begin{bmatrix} \{u^e\} \\ \{\omega^e\} \\ \{\theta^e\} \\ \{\psi^e\} \end{bmatrix} + \begin{bmatrix} [M^{11}] & [M^{12}] & [M^{13}] & [M^{14}] \\ [M^{21}] & [M^{22}] & [M^{23}] & [M^{24}] \\ [M^{31}] & [M^{32}] & [M^{33}] & [M^{34}] \\ [M^{41}] & [M^{42}] & [M^{43}] & [M^{44}] \end{bmatrix} \begin{bmatrix} \{u'^e\} \\ \{\omega'^e\} \\ \{\theta'^e\} \\ \{\psi'^e\} \end{bmatrix} = \begin{bmatrix} \{b^{1e}\} \\ \{b^{2e}\} \\ \{b^{3e}\} \\ \{b^{4e}\} \end{bmatrix} \qquad (39)$$

Where $\{[K^{mn}], [M^{mn}]\}$ and $\{\{U^e\}, \{\omega^e\}, \{\theta^e\}, \{\psi^e\}, \{U'^e\}, \{\omega'^e\}, \{\theta'^e\}, \{\psi'^e\} and \{b^{me}\}\}$ $(m, n = 1, , 2, 3, 4)$ denote the set of matrices of order 2×2 and 2×1 respectively and *prime* $(')$ indicates $\frac{d}{d\eta}$.

These matrices are defined as follows:

$$\begin{cases} K_{ij}^{11} = -S\int_{y_e}^{y_{e+1}} \left[\left(\chi_i^e\right)\left(\dfrac{\partial \chi_j^e}{\partial \eta}\right)\right] d\eta + \int_{y_e}^{y_{e+1}} \left[\left(\dfrac{\partial \chi_i^e}{\partial \eta}\right)\left(\dfrac{\partial \chi_j^e}{\partial \eta}\right)\right] d\eta + (A_1 + A_4 + A_5)\int_{y_e}^{y_{e+1}} \left[\left(\chi_i^e\right)\left(\chi_j^e\right)\right] d\eta, \\ K_{ij}^{12} = -A_3\int_{y_e}^{y_{e+1}} \left[\left(\chi_i^e\right)\left(\dfrac{\partial \chi_j^e}{\partial \eta}\right)\right] d\eta,\ K_{ij}^{13} = -Gr\int_{y_e}^{y_{e+1}} \left(\chi_i^e\right)\left(\chi_j^e\right) d\eta,\ K_{ij}^{14} = -Gm\int_{y_e}^{y_{e+1}} \left(\chi_i^e\right)\left(\chi_j^e\right) d\eta, \\ M_{ij}^{11} = \int_{z_e}^{z_{e+1}} \left(\chi_i^e\right)\left(\chi_j^e\right) d\eta,\quad M_{ij}^{12} = M_{ij}^{13} = M_{ij}^{14} = 0, \end{cases} \qquad (40)$$

$$\begin{cases} K_{ij}^{21}=0, K_{ij}^{22}=0, \\ K_{ij}^{23}=-S\int_{y_e}^{y_{e+1}}\left[\left(\chi_i^e\right)\left(\frac{\partial\chi_j^e}{\partial\eta}\right)\right]d\eta+\lambda\int_{y_e}^{y_{e+1}}\left[\left(\frac{\partial\chi_i^e}{\partial\eta}\right)\left(\frac{\partial\chi_j^e}{\partial\eta}\right)\right]d\eta, \quad K_{ij}^{24}=0, \\ M_{ij}^{21}=0, \quad M_{ij}^{232}=0, M_{ij}^{23}=\int_{y_e}^{y_{e+1}}\left(\chi_i^e\right)\left(\chi_j^e\right)d\eta, M_{ij}^{34}=0 \end{cases} \tag{41}$$

$$\begin{cases} K_{ij}^{31}=0, \\ K_{ij}^{32}=-S\int_{y_e}^{y_{e+1}}\left[\left(\chi_i^e\right)\left(\frac{\partial\chi_j^e}{\partial\eta}\right)\right]d\eta+A_6\int_{z_e}^{z_{e+1}}\left[\left(\frac{\partial\chi_i^e}{\partial\eta}\right)\left(\frac{\partial\chi_j^e}{\partial\eta}\right)\right]d\eta, \\ K_{ij}^{33}=-Ec\int_{y_e}^{y_{e+1}}\left(\chi_i^e\right)\left(\frac{\partial\overline{U}}{\partial\eta}\right)\left(\frac{\partial\chi_j^e}{\partial\eta}\right)d\eta, \\ K_{ij}^{34}=-Du\int_{y_e}^{y_{e+1}}\left(\frac{\partial\chi_i^e}{\partial\eta}\right)\left(\frac{\partial\chi_j^e}{\partial\eta}\right)d\eta, \\ M_{ij}^{31}=0, \ M_{ij}^{32}=0, M_{ij}^{33}=\int_{y_e}^{y_{e+1}}\left(\chi_i^e\right)\left(\chi_j^e\right)d\eta, \quad M_{ij}^{34}=0 \end{cases} \tag{42}$$

$$\begin{cases} K_{ij}^{41}=0, K_{ij}^{42}=0, K_{ij}^{43}=-Sr\int_{y_e}^{y_{e+1}}\left(\chi_i^e\right)\left(\frac{\partial\chi_i^e}{\partial\eta}\right)\left(\frac{\partial\chi_j^e}{\partial\eta}\right)d\eta, \\ K_{ij}^{44}=-S\int_{y_e}^{y_{e+1}}\left[\left(\chi_i^e\right)\left(\frac{\partial\chi_j^e}{\partial\eta}\right)\right]d\eta+\frac{1}{Sc}\int_{y_e}^{y_{e+1}}\left[\left(\frac{\partial\chi_i^e}{\partial\eta}\right)\left(\frac{\partial\chi_j^e}{\partial\eta}\right)\right]d\eta+\gamma\int_{y_e}^{y_{e+1}}\left(\chi_i^e\right)\left(\chi_j^e\right)d\eta, \\ M_{ij}^{41}=0, \quad M_{ij}^{42}=0, \ M_{ij}^{43}=\int_{y_e}^{y_{e+1}}\left(\chi_i^e\right)\left(\chi_j^e\right)d\eta, \ M_{ij}^{44}=0 \end{cases} \tag{43}$$

$$\begin{cases} b_i^{1e}=\left[\left(\chi_i^e\right)\left(\frac{\partial U}{\partial\eta}\right)\right]_{y_e}^{y_{e+1}}, \ b_i^{2e}=\left[\left(\chi_i^e\right)\left(\frac{\partial\omega}{\partial\eta}\right)\right]_{y_e}^{y_{e+1}}, \\ b_i^{3e}=\left[\left(\chi_i^e\right)\left(\frac{\partial\theta}{\partial\eta}\right)+Du\left(\chi_i^e\right)\left(\frac{\partial\psi}{\partial\eta}\right)\right]_{y_e}^{y_{e+1}}, b_i^{4e}=\left[\left(\chi_i^e\right)\left(\frac{\partial\psi}{\partial\eta}\right)+Sr\left(\chi_i^e\right)\left(\frac{\partial\theta}{\partial\eta}\right)\right]_{y_e}^{y_{e+1}} \end{cases} \tag{44}$$

A grid refinement test is carried out by dividing the whole domain into successively sized grids 81x81, 101x101 and 121x121 in the z-axis direction. Furthermore we ran the finite element code for different grid sizes and finally we found that all the solutions are independent of grid size. After many tests we adopted a grid size of 101 intervals. Thus all the computations were carried out with 101 intervals of equal step size 0.01. At each node 4 functions are to be evaluated and after assembly of element equations, a set of 404 non-linear equations are obtained which may not produce closed form solutions; consequently an *iterative scheme* is adopted to solve the system by introducing the boundary conditions. Finally the solution is assumed to be convergent whenever the relative difference between two successive iterations is less than the value 10^{-6}. Following computation of the principal variables i.e. velocity (U), angular velocity i.e. micro-rotation (ω), temperature function (θ) and concentration function (ψ), certain gradients of these functions are also evaluated. These physical quantities are the skin-friction, wall couple stress, Nusselt number and Sherwood number.

Skin-friction is obtained as,

$$C_f = \left[\frac{\partial U}{\partial \eta}\right]_{\eta=0} \tag{45}$$

Wall couple stress is defined as,

$$C_w = -\left[\frac{\partial \omega}{\partial \eta}\right]_{\eta=0} \tag{46}$$

Nusselt number is computed as,

$$Nu/\mathrm{Re}_x = -\left[\frac{\partial \theta}{\partial \eta}\right]_{\eta=0} \tag{47}$$

Sherwood number is evaluated as,

$$Sh/Re_x = -\left[\frac{\partial \psi}{\partial \eta}\right]_{\eta=0} \tag{48}$$

4. VALIDATION OF NUMERICAL RESULTS

With reference to the validity and accuracy of current numerical results the skin-friction, couple wall stress, Nusselt number and Sherwood number are compared with the results reported analytically by Kundu *et al*. [24] in the absence of the Hall current, heat absorption, viscous

dissipation, Dufour number and chemical reaction parameters and are presented quantitatively in **Table 1**. Very close correlation between the present finite element numerical results and the small perturbation solutions of Kundu *et al*. [24] is achieved. Therefore these favorable comparisons lend high confidence in the present finite element code accuracy.

5. RESULTS AND INTERPRETATION

The nonlinear boundary value problem solved in the previous section is dictated by an extensive number of thermal and hydrodynamic parameters. In order to gain a clear insight into the physical problem, numerical calculations for distribution of the translational velocity, microrotation (angular) velocity, temperature and concentration for different values of these parameters is conducted with graphical illustrations (**Figs. 2-29**). For the purpose of our computation, we adopted the following default parameters: $\varepsilon = 0.01$, $n = 10$, $t = 0.1$, $nt = \pi/2$, and all graphs therefore correspond to these values unless specifically indicated otherwise on the appropriate graph. The permeability in all the Figures plotted is set at 0.5 which corresponds to a highly porous regime, characteristic of many materials operations and working MHD generators. The value of *Pr* is taken to be 0.71 which corresponds to air at 20°C and 1 atmospheric pressure and the value of *Sc* is 0.6 (water-vapour). Due to the presence of free convection currents, large positive values of *Gr* = 10 and *Gm* = 5 are selected which imply strong thermal and species buoyancy effects in the regime and where the thermal buoyancy is twice the intensity of species buoyancy. Numerical values of the coefficients proportional to the skin friction C_f, couple stress coefficient C_w, Nusselt number Nu and Sherwood number Sh are given in **Table 2** for the general model with all parameters invoked.

It is evident that as Eringen micropolar vortex parameter (Δ), radiation parameter (F), Soret number (Sr) and Dufour number (Du) increase, the skin friction coefficient C_f and wall couple stress coefficient $-C_w$ *both increase*. However with greater suction parameter (*S*) and chemical reaction parameter (γ), the skin friction coefficient C_f and wall couple stress coefficient $-C_w$ both decrease. Also it is apparent that as wall suction (S), heat absorption parameter (Q_H), and

chemical reaction (γ) increases, a significant increase is computed in Sherwood number, Sh. Conversely with increasing Soret (thermo-diffusive) number, there is a reduction in Sherwood number Sh i.e. mass transfer rates at the plate surface are decreased. Furthermore with an increase in radiation parameter (F) and Dufour (diffuso-thermal) number (Du) increases, the Nusselt number (Nu) decreases i.e. wall heat transfer rates are reduced at the plate surface. Finally with an increase in rotational parameter (R) there is initially a substantial *increase* in skin friction C_f i.e. the flow is *strongly accelerated* in the vicinity of the plate; however with further increase in R there is a subsequent deceleration in the flow. However there is a consistent elevation in wall couple stress coefficient $-C_w$ with progressive increase in rotational parameter (R).

Figure 2 shows the pattern of the translational velocity for different values of magnetic field parameter, $M = \dfrac{\mu_e H_0}{U_r}\sqrt{\dfrac{\sigma \nu}{\rho}}$. It is to be noted that U is a composite velocity field which contains both original primary and secondary velocity components by virtue of complex variables. The parameter M arises solely in the transformed *linear momentum eqn*. (24) in the final two terms, $-\left(\dfrac{M^2}{1+m^2}+\dfrac{1}{K}\right)U - i\left(\dfrac{mM^2}{1+m^2}\right)U$. M is therefore also coupled with the Hall parameter, m. Both terms are drag forces which serve to inhibit the flow. It is observed that, adjacent to the surface of the plate, the translational velocity decreases with increase of M. The imposition of transverse magnetic field of strength, H_o, generates in the electrically-conducting micropolar fluid a resistive type force, called as Lorentz force, which acts against the relative motion of the fluid. This retarding force decelerates the fluid flow strongly. Similarly in fig. 3 an increase in magnetic parameter is observed to significantly decelerate the angular velocity i.e. reduce the magnitude of micro-rotation, although the effect is more localized at the plate surface and progressively decays further from the plate. The micro-rotation field is influenced indirectly via the deceleration in the linear (translational) velocity via the coupling terms in the composite linear momentum eqn. (24) i.e. $+i\Delta\dfrac{\partial \omega}{\partial \eta}$. Linear velocity terms do not arise however in the angular momentum composite eqn. (25). Increasing magnetic field therefore has a damping

effect on the global velocity and angular velocity fields and can therefore be exploited to control both. In both figs. 2 and 3 asymptotically smooth solutions are obtained indicating that a sufficiently large infinity boundary condition is prescribed in the free stream.

Figures 4 and 5 illustrate the influence of the Eringen vortex viscosity ratio parameter (Δ) on translational velocity and microrotation velocity profiles across the boundary layer. It is noteworthy that translational velocity distribution (fig. 4) is greater for a *weaker micropolar fluid* ($\Delta = 0.1$) as compared with *stronger micropolar fluid* ($\Delta = 0.4$) Micropolarity (i.e. increasing vortex viscosity of micro-elements) therefore consistently induces deceleration in the flow adjacent to the plate. All profiles are parabolic and peak at some distance from the wall, decaying smoothly to vanish in the free stream. Fig. 5 shows that the magnitude of micro-rotation velocity at the wall is also strongly decreased as Δ increases. The micro-rotation profiles decay consistently from the wall to the free stream i.e. the peak magnitude in micro-rotation (angular velocity) is always attained at the wall irrespective of the value of Δ. The presence of increasing concentration of micro-elements which enhances vortex viscosity therefore also damps the gyratory motions of micro-elements. The maximum influence is at the wall since with greater concentration of micro-elements, these micro-elements are physically impaired from rotating near the boundary more than anywhere else in the fluid regime. This effect is progressively reduced with distance from the plate.

Figures 6 and 7 respectively show the impact of the Hall current parameter (m) on the translational velocity (U) and micro-rotation (ω) distributions, respectively. A significant enhancement in velocity U accompanies an increase in values of m as depicted in fig 6. This is characteristic of Hall current and has been observed by other researchers and is documented also by Cramer and Pai [49]. This effect is however mainly attributable to the acceleration in the secondary flow rather than primary flow, which is expressed via the global velocity, U. Figure. 7, illustrates the influence of Hall parameter on micro-rotation profile. A significant depression is caused in micro-rotation with greater m values indicating that gyratory motions (angular velocities) are significantly damped with greater Hall effect. Micro-rotation values are therefore maximized with weak Hall current effect and minimized with strong Hall current effect.

Figures 8-11 present the response in velocity, micro-rotation, temperature and concentration to a variation in wall suction parameter (*S*). Fig. 8 shows that increasing suction significantly decreases velocity i.e. decelerates the boundary layer flow. Greater suction corresponds physically to removal of micropolar fluid via the wall. This destroys momentum, and causes the boundary layer to adhere to the wall thereby stabilizing boundary layer growth. due to which the velocity of the fluid decreases, i.e., the flow is decelerated. However, the opposite behavior is produced by the imposition of injection. The presence of wall suction therefore may be utilized to regulate flows and this has important implications in both magnetic materials processing and near-wall dynamics in MHD generators. We note that the case $S < 0$ corresponds to blowing (mass injection) at the wall and is not relevant to the current study and has therefore not been addressed. Overall the influence of suction is to *increase* momentum boundary layer thickness. Figure 9 indicates that micro-rotation is also significantly reduced with greater suction at the plate. The deceleration in the linear flow evidently also both the suction term, $-S\frac{\partial \omega}{\partial \eta}$ in eqn. (25) and via coupling with the angular momentum field (micro-rotation) retards gyratory motion (spin) of micro-elements which leads to a decrease in ω values. Again smooth convergence of profiles in the free stream demonstrates that a sufficiently large infinity boundary condition has been implemented in the numerical finite element code. Angular momentum boundary layer thickness therefore will also be *increased* with greater suction. Inspection of Figure 10 reveals that a marked decrease in the temperature of the fluid is also caused by an increase in wall suction. The removal of micropolar fluid from the boundary layer via the porous wall inhibits momentum diffusion. The suction term, $-S\frac{\partial \theta}{\partial \eta}$ in eqn. (26) also serves to suppress thermal diffusion in the regime. This cools the boundary layer and results in a *decrease* in thermal boundary layer thickness. Figure 11 shows that as the suction increases the concentration, ψ, decreases. As with all the flow variables, suction directly influences the concentration field also, this time via the term, $-S\frac{\partial \psi}{\partial \eta}$, in eqn. (27). As suction is applied the particles of the diffusing species are drawn closer to the plate. This results in a decrease of the concentration boundary layer thickness.

Figures 12-13 visualize the effect of the porous medium permeability parameter (*K*) on both velocity and microrotation fields. This parameter characterizes the hydrauic transmissivity of the porous medium. It arises in the Darcian drag force term in the composite linear momentum eqn. (24), viz $-\left(\frac{1}{K}\right)U$. With increasing permeability the regime solid fibers progressively decrease. The Darcian bulk impedance to flow is therefore also decreased. This results in an *acceleration* in the translational velocity, *U*, as observed in fig. 12. This behaviour is sustained across the boundary layer i.e. for all values of transverse co-ordinate, η. The implication for MHD energy generators is that the flow can be damped strategically via the introduction of a porous material in the flow zone and accelerated with higher permeability media. It is also apparent that micro-rotation i.e. angular velocity is enhanced with greater permeability parameter although the effect is prominent near the plate surface and is weakened with further distance into the boundary layer. Since the permeability parameter does not arise in the angular momentum conservation (boundary layer) eqn. (25) the accelerating effect on micro-rotation is sustained via the boost in linear momentum experienced through the coupling terms which link both linear and angular momentum fields. The increase in permeability implies greater void space in the porous medium. This allows an enhancement in gyratory motions as the micro-elements are afforded greater space in which to spin.

Figures 14-15 depict the evolution in translational velocity (*U*) with different thermal Grashof (*Gr*) and species Grashof (*Gm*) numbers. Both Grashof numbers arise solely in the thermal and species buoyancy terms in the normalized momentum conservation eqn. (24) i.e. $+Gr\theta, +Gm\psi$. Thermal Grashof number *Gr* is described here as quantifying the relative magnitude of the thermal buoyancy force and the opposing viscous hydrodynamic (frictional) force acting on the micropolar fluid. Physically positive, negative and zero $(i.e.,\ Gr>0, Gr<0\ and\ Gr=0)$ values of the thermal Grashof number represent the *cooling of the boundary surface (plate)*, *heating of the boundary surface* and *absence of free convection currents (i.e. pure forced convection only)*, respectively. The velocity profiles are invariably enhanced with an increase of *positive* thermal Grashof number (the only case studied). For *Gr >1* there is a dominance of buoyancy forces over the viscous forces, which in turn further accelerates the flow (fig. 14). Increasing thermal buoyancy is therefore assistive to momentum development and results in a *decrease* in momentum boundary layer thickness. Fig. 15 shows that an increase in species (solutal) Grashof

number *Gm* in fact generates an even greater acceleration in the flow and substantially elevates translational velocity (*U*) throughout the boundary layer. The increasing concentration gradient associated with higher Gm values accentuates the species buoyancy force which adds driving potential to the boundary layer flow and manifests again in acceleration and decreasing momentum boundary layer thickness. These trends are consistent with many other studies in the area of buoyancy-driven non-Newtonian convection and are further corroborated by Gebhart *et al.* [50] and Gorla [51].

Figure 16 illustrates the influence of Prandtl number (*Pr*) on temperature profiles. It is evident that an increase in the Prandtl number induces a significant reduction in the temperature and therefore cools the magnetic micropolar fluid regime, thereby *decreasing* thermal boundary layer thickness. Greater Prandtl numbers correspond to lower thermal conductivity of the fluid. Therefore as *Pr* increases, thermal conduction heat transfer is suppressed and this leads to a plummet in temperatures. With *Pr > 1* the momentum diffusion rate also exceeds the thermal diffusion rate in the fluid. Higher Prandtl number fluids may characterize non-Newtonian working fluids (low molecular weight polymeric suspensions) and therefore such fluids, which are accurately simulated by the Eringen micropolar model can be implemented to achieve better cooling in the regime.

Figures 17-18 illustrates the influence of radiation-conduction parameter (F) on the translational velocity (U) and temperature (θ). An increase in F values (fig. 17) tends to accelerate the translational velocity throughout the boundary layer region. Increasing F values correspond to a greater contribution of thermal radiation heat transfer relative to thermal conduction heat transfer (as $F = \frac{4T_\infty^3 \bar{\sigma}}{k\bar{k}}$). This energizes the boundary layer, boosts momentum diffusion and leads to an *acceleration* in the flow. The momentum boundary layer thickness is therefore *reduced*. This type of effect characterizes optically-thick flows using the Rosseland model, as confirmed experimentally and theoretically by Adunson and Gebhart [52]. Fig. 18 indicates that with an increase of F the temperature profiles increases and this also increases thermal boundary layer thickness. The F parameter arises solely in the dimensionless energy conservation eqn. (26), in the augmented thermal diffusion term, $\frac{1}{\Pr}\left(1+\frac{4F}{3}\right)\frac{\partial^2\theta}{\partial\eta^2}$. This serves to energize the flow with $F > 1$ for which thermal radiation contribution exceeds thermal

conduction contribution. The supplementary heat flux assists in thermal transfer between fluid molecules. The case $F = 0$ physically represents vanishing thermal radiation and purely thermal conduction heat transfer and is therefore associated with minimal temperatures in the system.

Figures 19-20 depicts the influence of heat generation parameter, Q_H, on translational velocity and temperature distribution, respectively in the flow. The heat absorption parameter Q_H appearing in (21) quantifies the amount of heat absorbed per unit volume which is given by $Q'(T'_w - T'_\infty)$, Q' being a constant coefficient, which may take as either positive or negative or zero (no heat source/sink). The source term represents heat absorption for $Q_H > 0$ and heat generation when $Q_H < 0$. Physically speaking, the presence of heat absorption (thermal sink) effects has the tendency to reduce the fluid temperature. This de-energizes the flow and also causes a strong deceleration i.e. net reduction in the fluid velocity, as observed in Fig. 19. Greater heat absorption (Q_H) clearly reduces the temperatures in the domain as observed in Fig. 20, and the effect is most prominent at the wall (plate surface).

Figures 21and 22 illustrate the influence of the Eckert number i.e. viscous dissipation parameter (*Ec*) on velocity and dimensionless temperature profiles. *Ec* expresses the relationship between the kinetic energy in the flow and the boundary layer enthalpy difference. It embodies the conversion of kinetic energy into *internal energy* by work done against the viscous fluid stresses. It is an important parameter for describing real working fluids in MHD energy generators and materials processing where dissipation effects are not trivial. Positive Eckert number corresponds to cooling of the wall (plate) and therefore a transfer of heat from the plate to the micropolar fluid. Convection is enhanced and we observe in consistency with that the fluid is accelerated i.e. linear (translational) velocity is increased in the micropolar fluid. Temperatures are also enhanced markedly with greater Eckert number, as shown in Figure 22 since internal energy is increased due to kinetic energy dissipation.

Figures 23-24 depict the evolution in translational velocity and temperature function, respectively, with different values of diffuso-thermal parameter i.e. the *Dufour number*, $D_u = \frac{\kappa^2 K_T m_w}{q_w \rho c \mu}$. The Dufour effect refers to heat flux produced by a concentration (solutal) gradient. The fluid velocity increases with increase in Dufour number as seen in fig. 23. The augmented heat flux via the concentration field, therefore results in a thinning in the momentum

boundary layer (acceleration). Increasing diffusion-thermo parameter (Du) also accentuates the temperature profiles as shown in Figure 24. The temperature profiles in the presence of the Dufour effect are higher in comparison to in the absence of Dufour effect. The Dufour cross-diffusion term, $+D_u \frac{\partial^2 \psi}{\partial \eta^2}$ in the energy (heat) conservation eqn. (26) encourages diffusion of heat in the boundary layer via the solutal (concentration) gradient. The boundary layer flow is therefore energized with increasing Dufour number and thermal boundary layer thickness increases considerably in the presence of strong Dufour effects.

Figure 25 illustrates the response of concentration profiles (Ψ) to different values of Schmidt number (Sc). The Schmidt number is a fundamental parameter in species diffusion (mass transfer) which describes the ratio of the momentum to the molecular (species) diffusivity. The Schmidt number therefore quantifies the relative effectiveness of momentum and mass transport by diffusion in the hydrodynamic (velocity) and concentration (species) boundary layers. For $Sc > 1$ momentum diffusion rate *exceeds* the species diffusion rate. The opposite applies for $Sc < 1$. For $Sc = 1$ both momentum and concentration (species) boundary layers will have the same thickness and diffusivity rates will be equal. It is observed that as the Schmidt number increases the concentration decreases. The associated decrease in species diffusivity results in less vigorous mass transfer which reduces concentration levels and also depletes the concentration boundary layer thickness. Selection of specific materials with particular molecular diffusivities therefore has a critical impact on the diffusion process in micropolar liquids and again this is an important consideration in materials processing operations where the distribution of species in fluids can be manipulated to achieve more homogenous patterns.

Figures 26-27 present the effect of thermo-diffusive parameter i.e. Soret number which is defined as $Sr = \frac{D_m K_T \, q_w}{\kappa \, m_w}$, on the translational velocity and concentration distributions, respectively. The Soret effect arises where small light molecules and large heavy molecules separate under a temperature gradient. Usually this effect is important where more than one chemical species is present under a very large temperature gradient such as CVD (chemical vapor deposition) in polymer materials processing [53], chemical reactors and energy generators. Figure 26 shows that a substantial elevation in translational velocity is induced with increasing of

Sr and therefore thermo-diffusion *assists momentum development* in the boundary layer, leading to a decrease in momentum boundary layer thickness. A marked enhancment in concentration profiles increases significantly with an increase of Soret number Sr. The Soret cross-diffusion term in the species conservation eqn. (27) i.e. $+Sr\left(\frac{\partial^2\theta}{\partial\eta^2}\right)$, encourages diffusion of solute in the boundary layer via the thermal gradient. This results in a significant increase in concentration boundary layer thickness.

Finally Figures **28-29** illustrate the evolution in translational velocity (U) and concentration (Ψ) with a change in chemical reaction parameter (γ). The reaction parameter is based on a first-order irreversible chemical reaction which takes place both in the bulk of the fluid (homogeneous) as well as at plate which is assumed to be catalytic to chemical reaction. Although chemical reactions generally fall into one of two categories i.e. *homogenous* or *heterogenous*, the former is of interest in the present study. Homogenous chemical reactions take place uniformly throughout a given phase and are similar in nature to an internal source of heat generation. We consider the destructive type of homogenous chemical reaction. Increasing γ values are found, in fig. 28, to instigate a considerable reduction in the velocity i.e. flow deceleration. The momentum boundary layer thickness is therefore also decreased substantially with greater chemical reaction effect. Fig. 29 shows that concentration is also depleted in the boundary layer with greater chemical reaction, since more species is destroyed via the chemical reaction. This results in a reduction in the thickness of the concentration boundary layer. These trends for the magnetic micropolar fluid concur closely with other studies including, for example, Das *et al.* [54].

6. CONCLUDING REMARKS

In this work, motivated by applications in non-Newtonian electro-conductive materials processing and MHD energy generator systems, a multi-physico-chemical model has been developed for *unsteady hydromagnetic free convection flow of an incompressible, micropolar fluid from a rotating plate in porous media*. Viscous heating, homogenous chemical reaction, wall mass flux (suction), Hall current, Soret and Dufour cross-diffusion effects have been

incorporated into the model. The transformed conservation equations for momentum, angular momentum, energy and species have been normalized with appropriate variables. The resulting nonlinear, unsteady partial differential coupled boundary value problem has been solved numerically, under initial and boundary conditions, via a variational finite element method with a Galerkin weighted residual scheme. Validation for solutions for selected cases has been conducted with earlier studies i.e. Kundu *et al.* [24] and excellent correlation achieved, testifying to the accuracy of the present numerical code. The finite element solutions for the thermofluid variables have been presented graphically and a parametric study performed to elucidate the influence of all key hydrodynamic, magnetic, thermal and non-Newtonian parameters emerging in the formulation. The main findings of the present investigation may be summarized as follows:

(i) The *flow is decelerated* and *momentum boundary layer thickness increased* of the magneto-micropolar fluid field with increasing values of *Eringen vortex viscosity parameter, magnetic body force parameter, wall suction parameter, heat absorption parameter and chemical reaction parameter.*

(ii) The *flow is accelerated* and *momentum boundary layer thickness decreased* of the magneto-micropolar fluid field with increasing values of Hall current parameter, permeability parameter, thermal Grashof number and species Grashof number, radiation parameter, Eckert number, Dufour number and Soret number.

(iii) Angular velocity (micro-rotation) is *suppressed* and micro-rotation boundary layer thickness increased with *increasing* magnetic body force parameter, Eringen micropolar vortex viscosity parameter, Hall parameter and wall suction parameter.

(iv) Angular velocity (micro-rotation) is *enhanced* and micro-rotation boundary layer thickness decreased with *increasing* porous medium permeability parameter.

(v) The *temperature* of the magneto-micropolar fluid and thermal boundary layer thickness are both *decreased* with *increasing* suction parameter, Prandtl number and heat absorption parameter.

(vi) The *temperature* of the magneto-micropolar fluid and thermal boundary layer thickness are *both increased* with *increasing* radiation-conduction parameter, Eckert number and Dufour number.

(vii) The *concentration magnitudes* of solute in the magneto-micropolar fluid and the concentration boundary layer thickness are decreased with increasing wall suction, Schmidt number and chemical reaction parameter.

(viii) The *concentration magnitudes* of solute in the magneto-micropolar fluid and the concentration boundary layer thickness are *increased* with increasing Soret number.

(ix) Sherwood number (wall mass transfer rate) is *reduced* with increasing Soret (thermo-diffusive) number.

(x) Nusselt number (wall heat transfer rate) is *decreased* with an increase in radiation parameter and Dufour (diffuso-thermal) number.

(xi) With an increase in rotational parameter there is initially a significant elevation in wall skin friction (flow *acceleration*); however with further increase in rotation (i.e. Coriolis body force) there is a subsequent deceleration in the flow.

(xii) With greater rotational parameter an enhancement in wall couple stress coefficient (micro-rotation gradient at the plate surface) is sustained.

The current simulations have shown the strong potential of finite element methods in simulating realistic transport phenomena in magnetic rheo-materials processing. Further studies will investigate alternate non-Newtonian models e.g. dusty two-phase models and will be communicated imminently.

REFERENCES

[1] Eringen, A.C., (1964) *Simple microfluids*, Int. J. Engng. Sci., 2, pp. 205-217.

[2] Eringen, A.C., (1972) *Theory of micropolar fluids*, J. Math. Mech,. 16, pp.1-18.

[3] Airman, T, Turk, M.A. and Sylvester, N.D., (1973) Micro-continuum fluid mechanics-review, *Int. J. Engineering Science*, 11, pp. 905-930.

[4] Airman, T, Turk, M.A. and Sylvester, N.D., (1973) Applications of Micro continuum fluid mechanics, *Int. J. Engineering Science*, 12, pp. 905-930.

[5] Lukaszewicz, G., (1999) *Micropolar fluids-Theory and Applications,* Birkhauser, Boston.

[6] Khatak, P. and Garg, H.C., (2012) Influence of micropolar lubricant on bearings performance: A review, *Proc. IMechE Part J: J Engineering Tribology*, 226, pp. 775–784.

[7] Latiff, N.A. Uddin, M.J. Anwar Bég, O. and Ismail, A.I.M., (2015) Unsteady forced bio convection slip flow of a micropolar nanofluid from a stretching/ shrinking sheet, *Proc. IMECHE- Part N: J. Nanoengineering, Nanomaterials and Nanosystems* (11 pages). DOI: 10.1177/1740349915613817.

[8] Zadravec, M. Hriberšek, M. and Škerget, L., (2007) Micropolar fluid flow modelling using the boundary element method, *Computational Methods in Multiphase Flow IV*, WIT Transactions on Engineering Sciences, 56, pp. 325 -332.

[9] Ali, N. Zaman, A. and Anwar Bég, O., (2015) Numerical simulation of unsteady micropolar hemodynamics in a tapered catheterized artery with a combination of stenosis and aneurysm, *Medical and Biological Engineering and Computing*. DOI: 10.1007/s11517-015-1415-3 (13pages).

[10] Jangili, S. and Murthy, J.V., (2015) Thermodynamic analysis for the MHD flow of two immiscible micropolar fluids between two parallel plates, *Front. Heat Mass Transfer*, 6(1), pp. 1–11.

[11] Tsai, R. and Huang, J.S., (2009) Numerical study of Soret and Dufour effects on heat and mass transfer from natural convection flow over a vertical porous medium with variable wall heat fluxes, *Computational Materials Sciences*, 47, pp. 23-30.

[12] Chien, C.P. and Mattes, B.L., (1983) Thermal Soret diffusion in the liquid phase epitaxial growth of binary III-V compounds, *J. Vac. Sci. Technol*.**,** B 1, 648.

[13] Blums, E. and Mezulis, A. (2010) Thermal diffusion and particle separation in ferrocolloids, *Transfer phenomenon in a magnetohydrodynamic and Electroconducting flows, Fluid Mechanics and its Applications*, 51**,** pp. 1-14.

[14] Yadav, D. Nam, D. and Lee, J., (2016) The onset of transient Soret-driven MHD convection confined within Hele-Shaw cell with nanoparticles suspension, *J. Taiwan Institute of Chemical Engineers*, 58, pp. 235–244.

[15] Dakhlia, R.B. Giovangigli, V. and Rosner, D.E., (2002) Soret effects in laminar counter flow spray diffusion flames, *Combust theory modelling*, 6, pp. 1-10.

[16] Fan Yang, Law, C.K. Sung, C.J. and Huiqiang Zhang., (2009) A mechanistic study of soret diffusion in hydrogen-air flames, *47th AIAA Aerospace Sciences Meeting, New Horizons Forum and Aerospace Exposition, Orlando, Florida, USA*.

[17] Postelnicu, A.,(2004) Influence of a magnetic field on heat and mass transfer by natural convection from vertical surface in porous media considering Soret and Dufour effects, *Int. J. Heat Mass Transfer*, 47, pp. 1467-1472.

[18] Alam, M.S. and Rahman, M.M., (2005) Dufour and Soret effects on MHD free convective heat and mass transfer flow past a vertical flat plate embedded in porous medium, *J. Naval Architecture and Marine Engineering*, 21, pp. 55-65.

[19] Vasu, B. Bhaskar Reddy, N. Ramachandra Prasad, V. and Anwar Bég, O., (2013) Thermo-diffusion and Diffusion-Thermo effects on free convection flow past a semi-infinite vertical plate in the presence of suction and injection, *Int. J. Energy & Technology*, 5(14), pp. 1-11.

[20] Anwar Bég, O. Bakier, A.Y. and Prasad, V.R., (2009) Numerical study of free convection magnetohydrodynamic heat and mass transfer from a stretching surface to saturated porous medium with Soret and Dufour effects, *Computational Materials Science*, 46(1), pp. 57-65.

[21] Partha, M.K. Murthy, P.V.S.N. and Sekhar, G.P.R., (2006) Soret and Dufour effects in a non-Darcy porous medium, *ASME J. Heat Transfer*, 128, pp. 605-610.

[22] Anwar Bég, O. Bhargava, R. Rawat, S. and Khaya, E., (2008) Numerical study of micropolar convective heat and mass transfer in a non-Darcy porous regime with Soret and Dufour effects, *Emirates J. Engineering Reaserch*, 13, pp. 51-66.

[23] Anwar Bég, O. Prasad, V.R., Vasu, B. Bhaskar Reddy, N. Li, Q. and Bhargava, R.,(2011) Free Convective heat and mass transfer from an isothermal sphere to a micropolar regime with Soret/Dufour effects, Int. J. Heat and mass Transfer, 54, pp. 9-18.

[24] Kundu, P.K. Das, K. and Jana, S.,(2015) MHD micropolar fluid flow with thermal radiation and thermal diffusion in rotating frame, *Bulletin Malaysia Mathematical Sciences Society*, 38, pp. 1185-1205.

[25] Ashraf, B. Hayat, T. and Alhuthali, M., (2015) Three-dimensional flow of Maxwell fluid with Soret and Dufour Effects, *ASCE J. Aerosp. Eng.*, 10.1061, AS.1943-5525.0000551, 04015065.

[26] Chen, J. Liang, C. and Lee, J.D., (2012) Micropolar electromagnetic fluids: control of vortex shedding using imposed transverse magnetic field, *J. Advanced Mathematics and Applications*, 1, pp. 151-162.

[27] Kim. Y.J., (2004) Heat and mass transfer in MHD micropolar flow over a vertical moving plate in a porous medium, *Transport Porous Media*, 56, pp.17-37.

[28] Borrelli, B. Giantesio, G. and Patria, M.C., (2015) MHD orthogonal stagnation-point flow of a micropolar fluid with the magnetic field parallel to the velocity at infinity, *Applied Math. Comp*, 264, pp. 44-60.

[29] Rawat, S. Bhargava, R. Renu Bhargava. and Anwar Bég, O., (2009) Transient magneto-micropolar free convection heat and mass transfer through a non-Darcy porous medium channel with variable thermal conductivity and heat source effects, *Proc.IMechE Part C- J. Mechanical Engineering Science*, 223, pp. 2341-2355.

[30] Zueco, J. Anwar Bég, O. Takhar, H.S., (2009) Network numerical analysis of magneto-micropolar convection through a a vertical circular non-Darcian porous medium conduit, *Computational Materials Science*, 46(4), pp. 1028-1037.

[31] Anwar Bég, O. Zueco, J. and Chang, T.B.,(2010) Numerical analysis of hydromagnetic gravity driven thin film micropolar flow along an inclined plane, *Chemical Engineering Communications*, 198 (3), pp. 312-331.

[32] Vafeas, P. Ploycarpos, P. Papadopoulos. Pavlos, M.H., (2009) Micropolar flow under the effect of a magnetic dipole, *AIP Conf. Proc*. 1148, 566. http://dx.doi.org/10.1063/1.322676.

[33] Anwar Bég, O. Rashidi, M.M. Bég, T.A. and Asadi, M., (2012) Homotopy analysis of transient magneto-bio-fluid dynamics of micropolar squeeze film: *a model for magneto-bio-rheological lubrication, J. Mechanics in Medicine and Biology*, 12, 1250051-1 to 1250051-21.

[34] Cowling, T.G., (1957) *Magnetohydrodynamics*, Wiley inters Science, New York.

[35] Takhar, H.S. Chamkha, A.J. and Nath, G.,(2002) MHD flow over a moving plate in a rotating fluid with magnetic field, hall currents and free stream velocity, *Int. J. Engineering Science*, 40, pp. 1511-1527.

[36] Ghosh, S.K. Anwar Bég, O. Zueco, J. and Prasad, V. R., (2010) Transient hydromagnetic flow in a rotating channel permeated by an inclined magnetic field with magnetic induction and Maxwell displacement current effects, *ZAMP: J. Applied Mathematics and Physics*, 61, pp. 147-169.

[37] Seth, G.S. Sharma, R. and Hussain, S.M., (2014) Hall effects on unsteady MHD natural convection flow of heat absorbing fluid past an accelerated moving vertical plate with Ramped temperature, *Emirates J. Engineering Research*, 19, pp. 19-32.

[38] Siva Reddy, S. and Shamshuddin, MD., (2015) Heat and mass transfer on the MHD flow of a micropolar fluid in the presence of viscous dissipation and chemical reaction. International Conference on Heat and Mass Transfer, *Procedia Engineering*, Vol.127, pp.885-892.

[39] Pal, D. and Talukdar, B., (2012) Perturbation technique for unsteady MHD mixed convection periodic flow, heat and mass transfer in micropolar fluid with chemical reaction in the presence of thermal radiation, *Central European J. Physics*, 10, pp. 1150-1167.

[40] Eringen, A.C., (2001) *Micro-Continuum Field Theories II: Fluent Media*, Springer, New York, USA.

[41] Anwar Bég, O. Rashidi, M.M. and Bhargava, R., (2011) *Numerical Simulation in Micropolar Fluid Dynamics*, Lambert: Sarbrucken, Germany.

[42] Ganapathy, R., (1994) A note on oscillatory Couette flow in a rotating system, *ASME J. Applied Mechanics*, 61, pp. 208-209.

[43] Brewster, M.Q., (1992) *Thermal Radiative Transfer and Properties*, John Wiley, New York.

[44] Anwar Bég, O., (2012) Numerical methods for multi-physical magnetohydrodynamics, *New Developments in Hydrodynamics Reaserch, Maximiano J. Ibragimov and A. Anisimov, Eds.,* Ch.1, pp. 1-110, Nova Science: New York.

[45] Anwar Bég, O. Bég, T.A. Bhargava, R. Rawat, S. and Tripathi, D., (2012) Finite element study of pulsatile magneto-hemodynamic non-Newtonian flow and drug diffusion in a porous medium channel, *J. Mechanics in Medicine and Biology*, 12(4), pp. 1250081.1-1250081.26.

[46] Rana, P. Bhargava, R. and Anwar Beg, O., (2013) Finite element simulation of unsteady MHD transport phenomenon on a stretching sheet in a rotating nanofluid, *Proc. IMECHE-Part N; J. Nanoengineering and Nanosystems*, 227, pp.77-99.

[47] Swapna, G. Kumar, L. Anwar Bég, O. and Singh, B., (2014) Finite element analysis of radiative mixed convection magneto-micropolar flow in a Darcian porous medium with variable viscosity and convective surface condition, *Heat Transfer-Asian Research*. DOI: 10.1002/htj.21134.

[48] Rana, P. Bhargava, R. Anwar Bég, O. and Kadir, A., (2016) Finite element analysis of viscoelastic nanofluid flow with energy dissipation and internal heat source/sink effects, *Int. J. Applied Computational Mathematics*, DOI:10.1007/s40819-016-0184-5 (27 pages).

[49] Cramer, K.R. and Pai, S.I., (1973) *Magnetofluid Dynamics for Engineers and Applied Physicists*, McGraw Hill, New York, USA.

[50] Gebhart, B. *et al*., (1988) *Buoyancy-Induced Flows and Transport*, Hemisphere, Washington, USA.

[51] Gorla, R.S.R., (1988) Combined forced and free convection in micropolar boundary layer flow on a vertical flat plate, *Int. J. Engineering Science*, 26, pp.385-391.

[52] Adunson, T. and Gebhart, B., (1972) An experimental and analytical study of natural convection with appreciable thermal radiation effects, *J. Fluid Mechanics*, 52, pp. 57–95.

[53] Jiang, B.T. and Chan, P.K., (2007) Effect of concentration gradient on the morphology development in polymer solutions undergoing thermally induced phase separation, *Macromolecular Theory and Simulations*, 16(7), pp. 690 – 702.

[54] Das, U.N. Deka, R. Soundalgekar, V.M., (1994) Effects of mass transfer on flow past an impulsively started infinite vertical plate with constant heat flux and chemical reaction, Forsch. *Ingenieurwes*., 60, pp. 284-287.

FIGURES

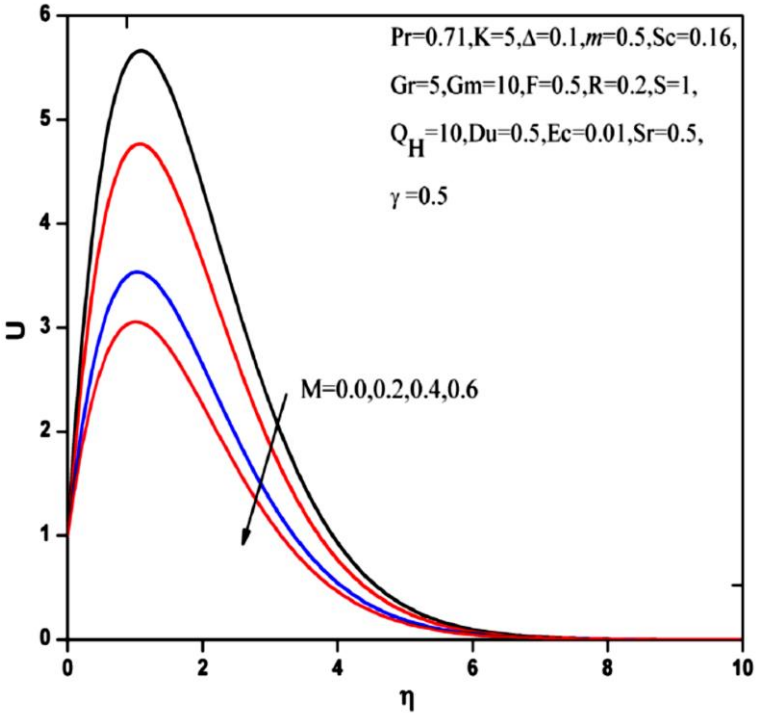

Fig. 2: Effect of magnetic body force parameter (*M*) on velocity.

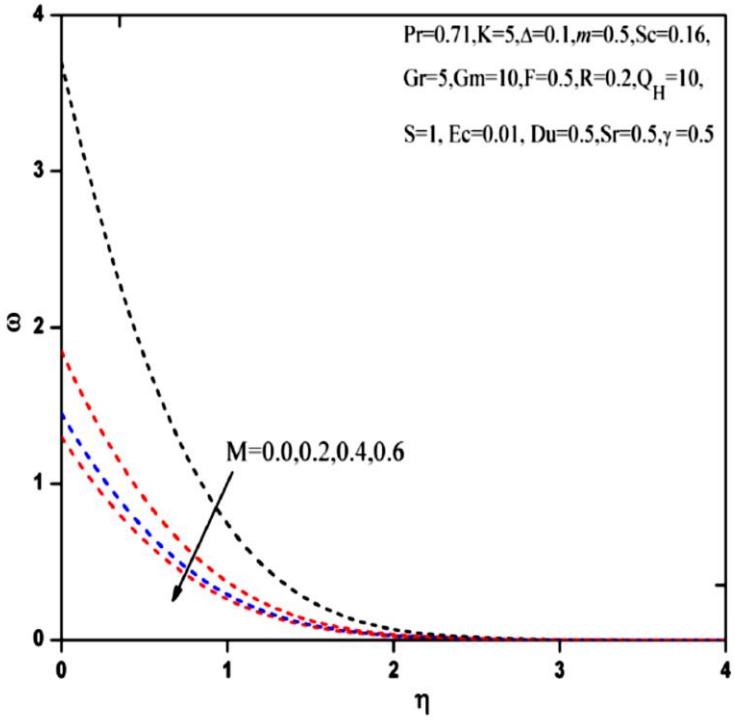

Figure 3: Effect of magnetic body force parameter (*M)* on angular velocity (micro-rotation).

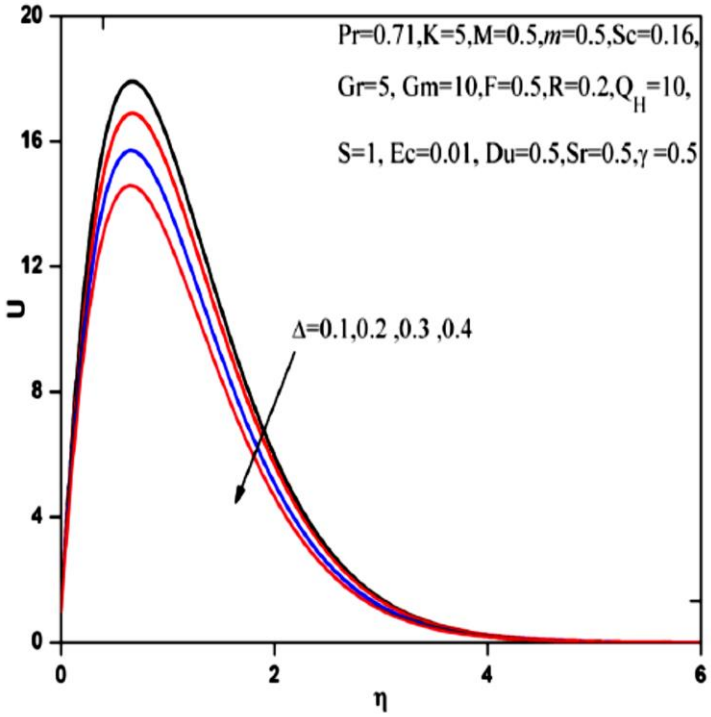

Figure 4: Effect of Eringen vortex viscosity parameter (Δ) on velocity.

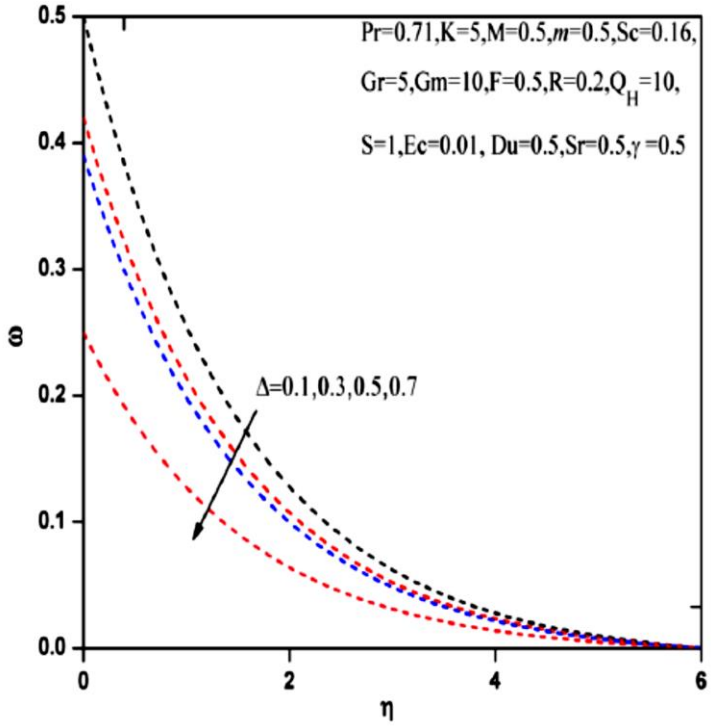

Figure 5: Effect of Eringen vortex viscosity parameter (Δ) on micro-rotation.

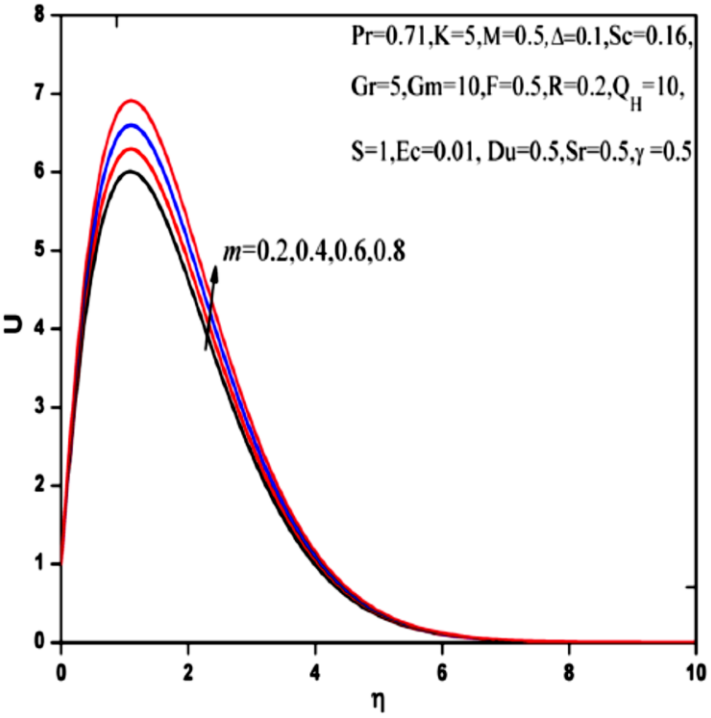

Figure 6: Effect of Hall parameter (m) on velocity

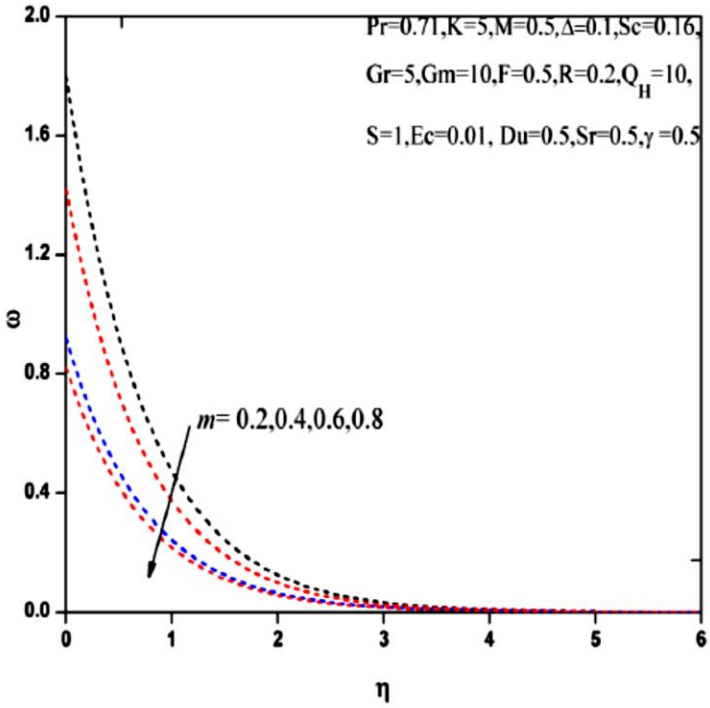

Figure 7: Effect of Hall parameter (*m*) on angular velocity (micro-rotation).

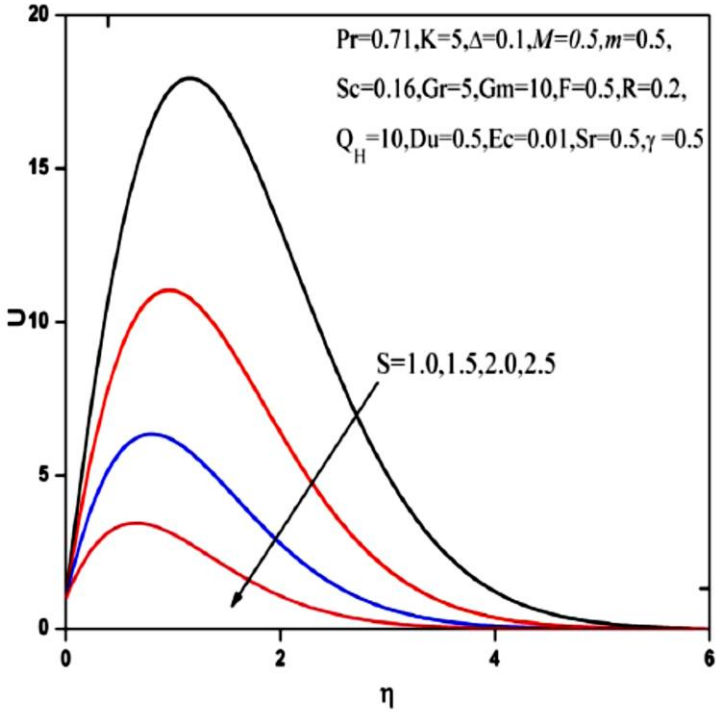

Figure 8: Effect of wall suction parameter (*S*) on velocity

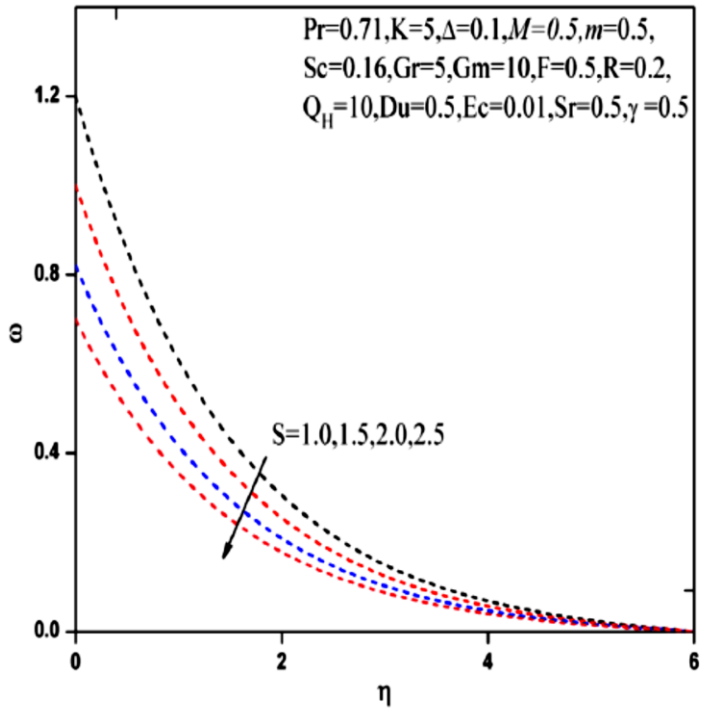

Figure 9: Effect of wall suction parameter (*S*) on angular velocity (micro-rotation)

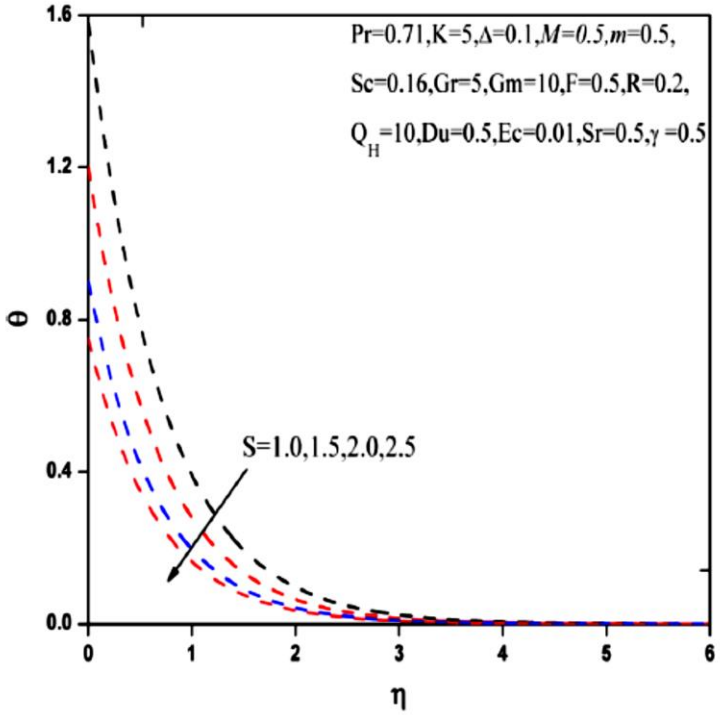

Figure 10: Effect of wall suction parameter (*S*) on temperature.

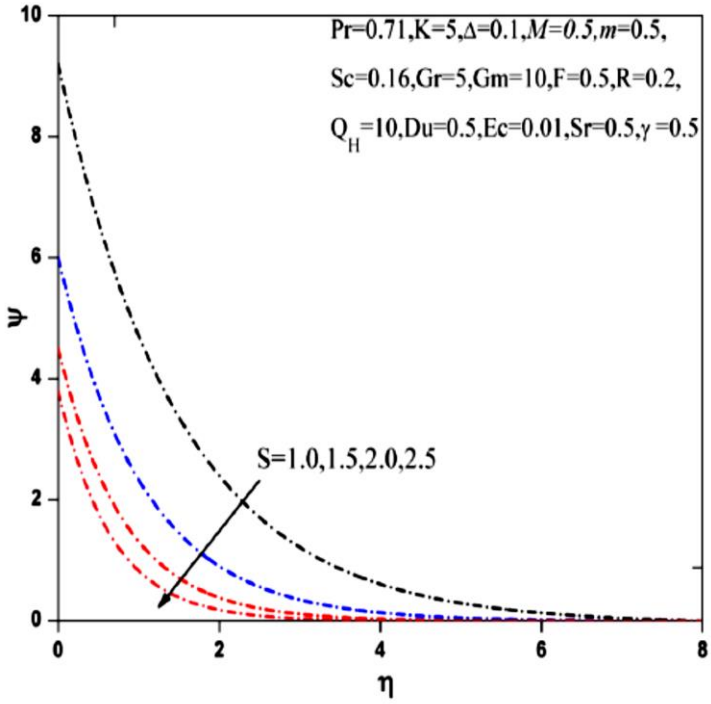

Figure 11: Effect of wall suction parameter (*S*) on species concentration.

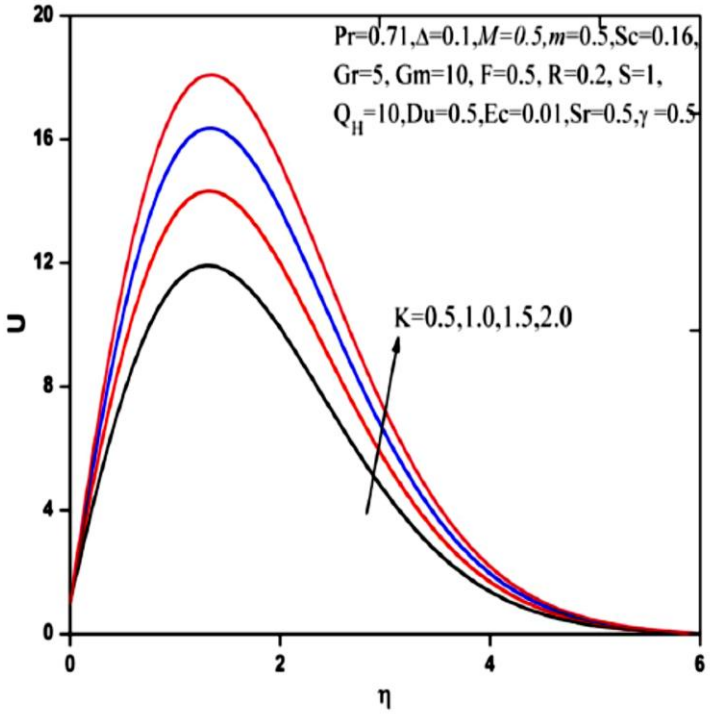

Figure 12: Effect of permeability parameter (*K*) on velocity.

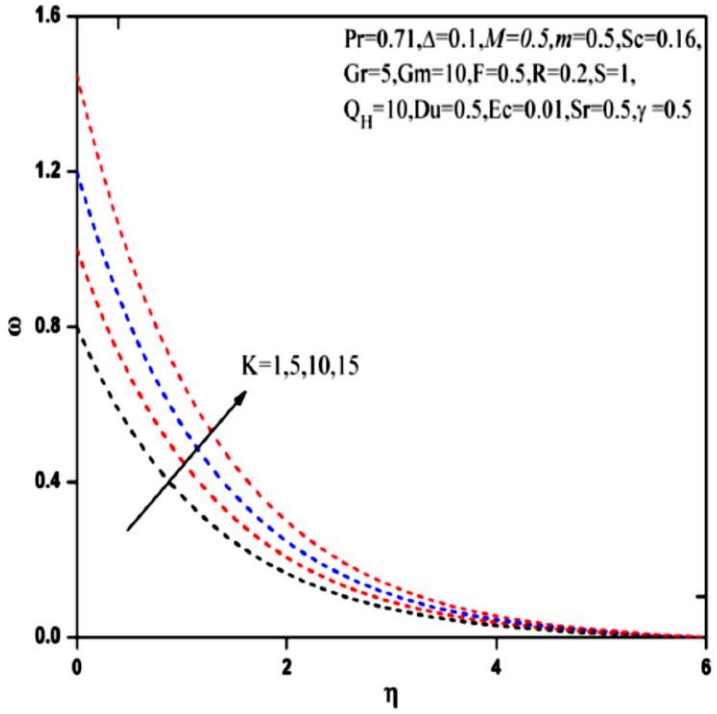

Figure 13: Effect of permeability parameter (*K*) on micro-rotation.

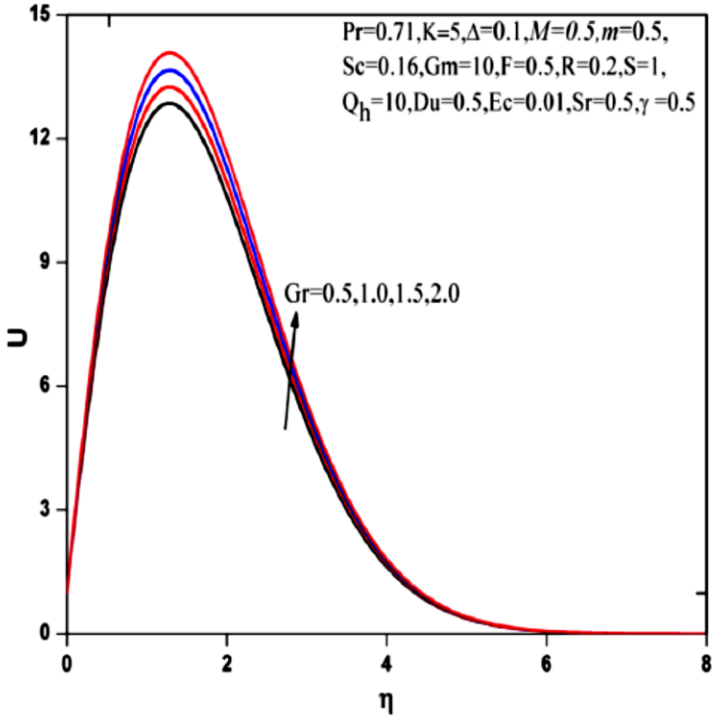

Figure 14: Effect of thermal Grashof number (*Gr*) on velocity.

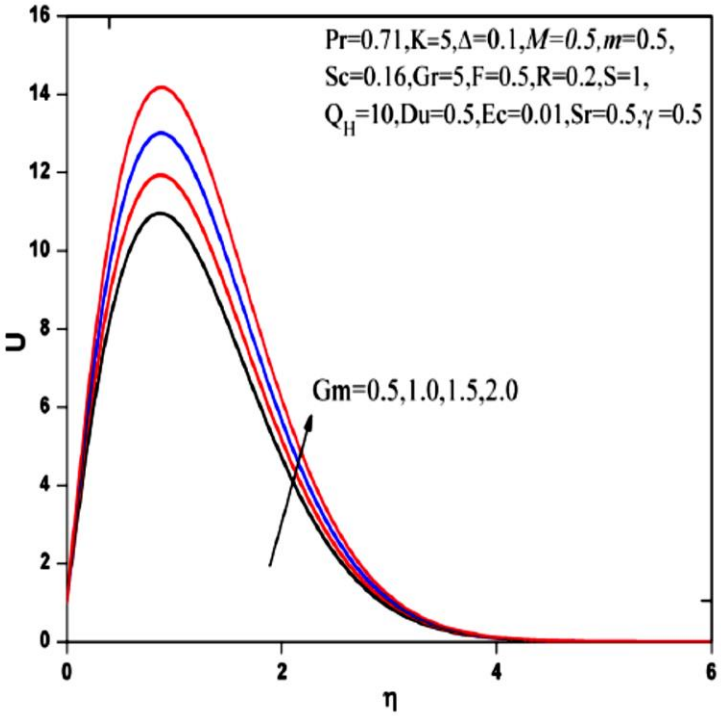

Figure 15: Effect of species (solutal) Grashof number (*Gm*) on velocity.

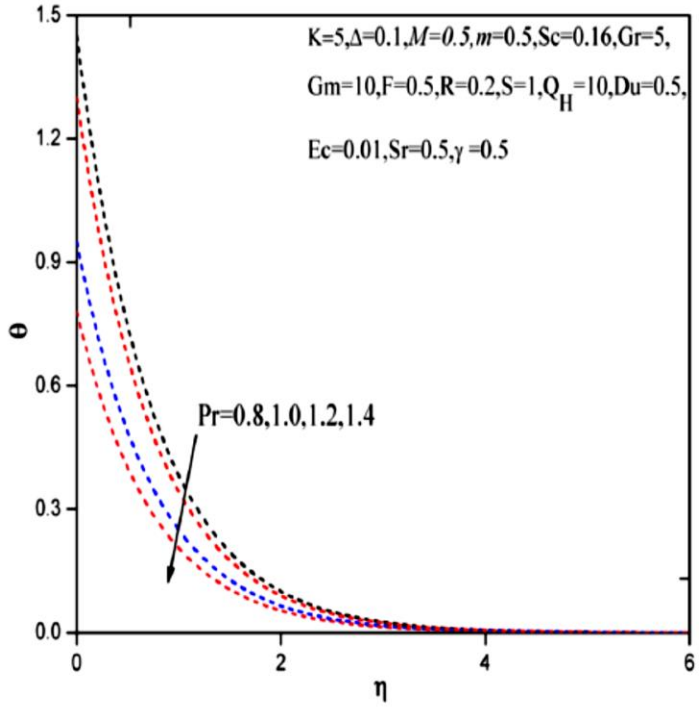

Figure 16: Effect of Prandtl number (*Pr*) on temperature

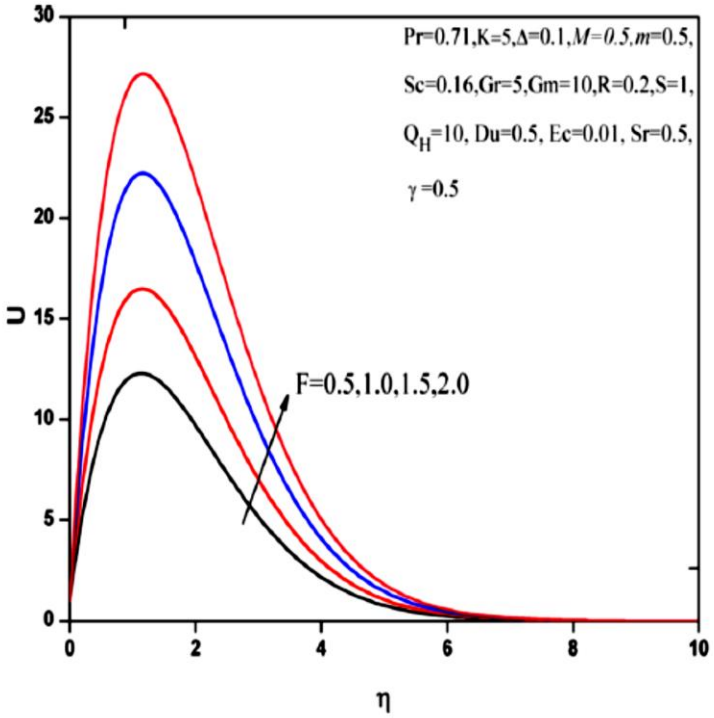

Figure 17: Effect of radiation parameter (*F*) on velocity.

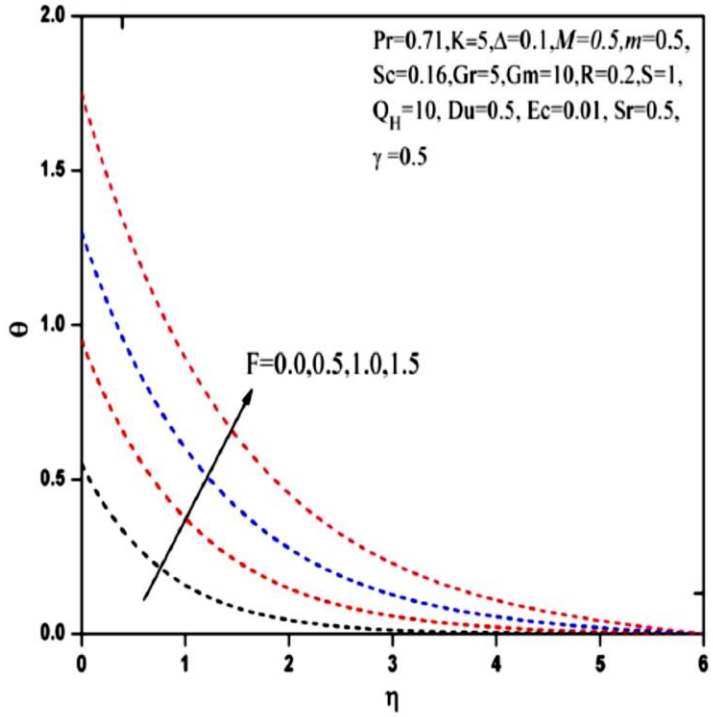

Figure 18: Effect of radiation parameter (*F*) on temperature.

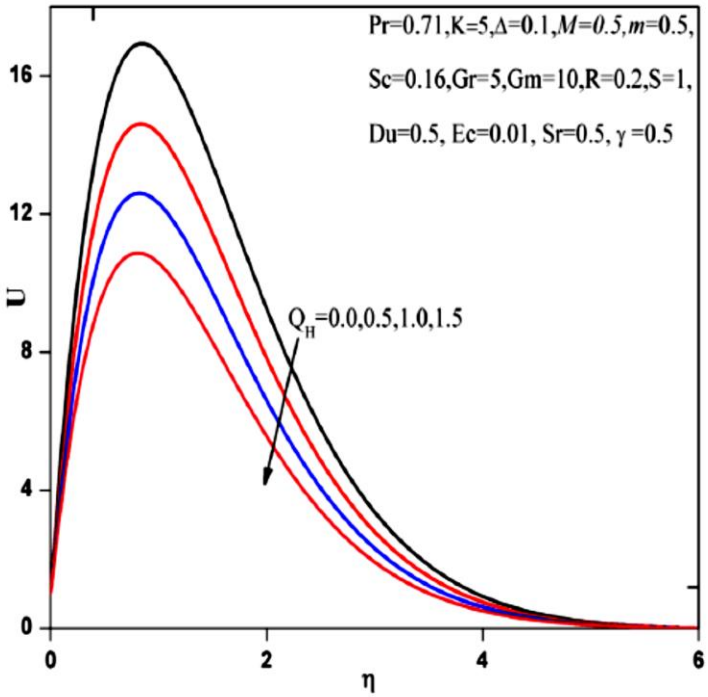

Figure 19: Effect of heat absorption parameter (Q_H) on velocity.

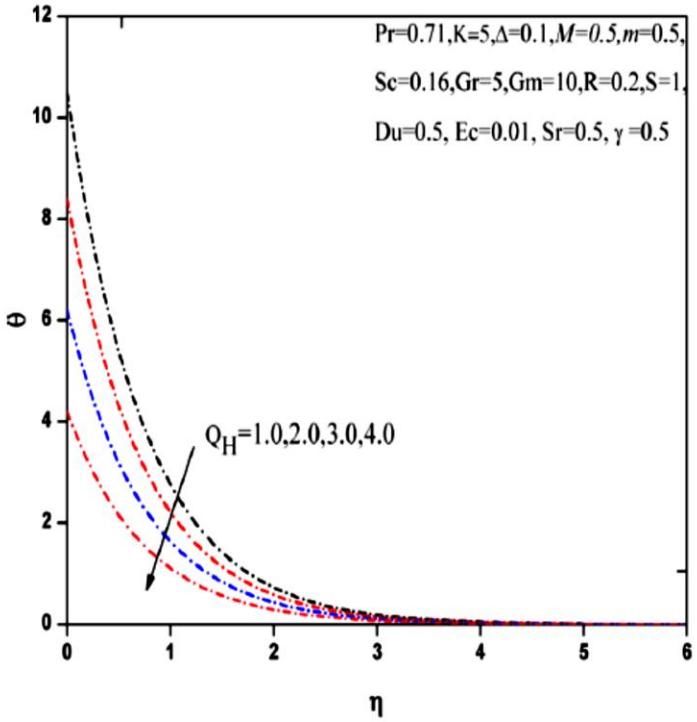

Figure 20: Effect of heat absorption parameter (Q_H) on temperature.

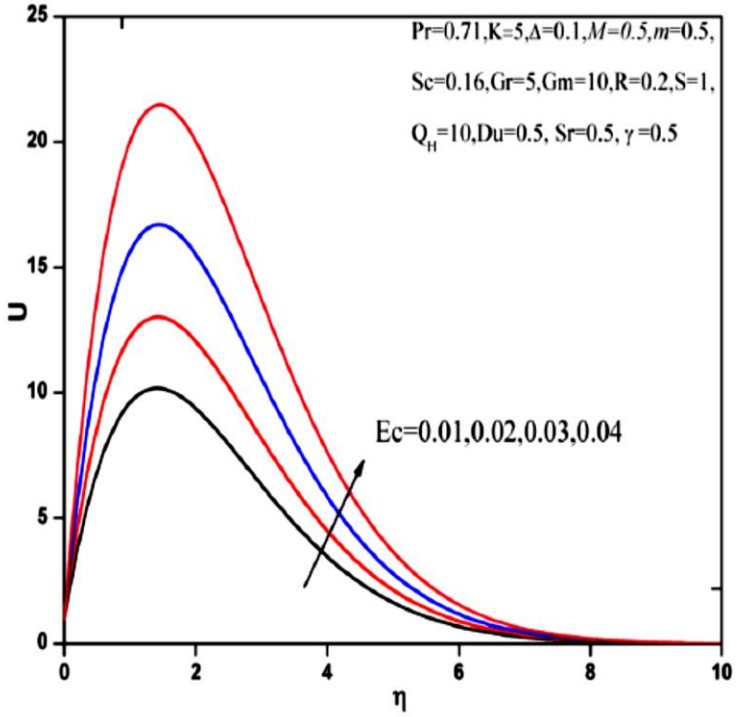

Figure 21: Effect of Eckert number (*Ec*) on velocity.

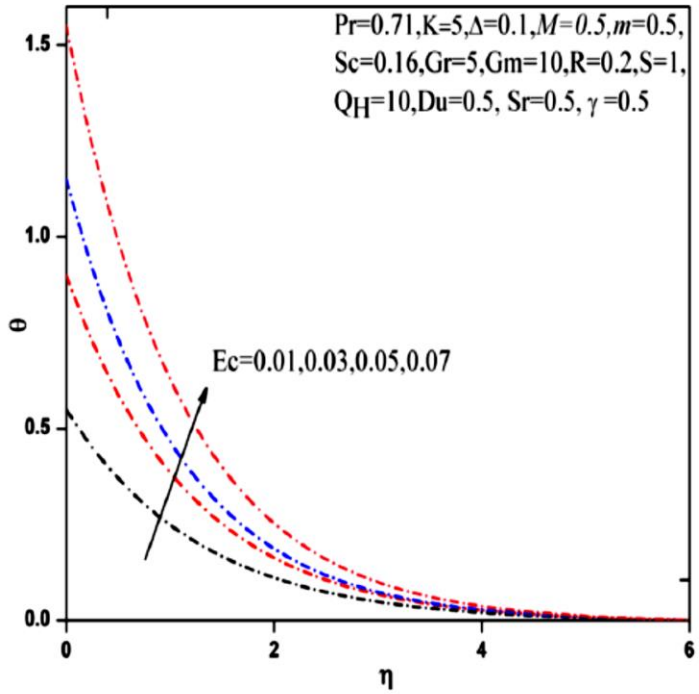

Figure 22: Effect of Eckert number (*Ec*) on temperature.

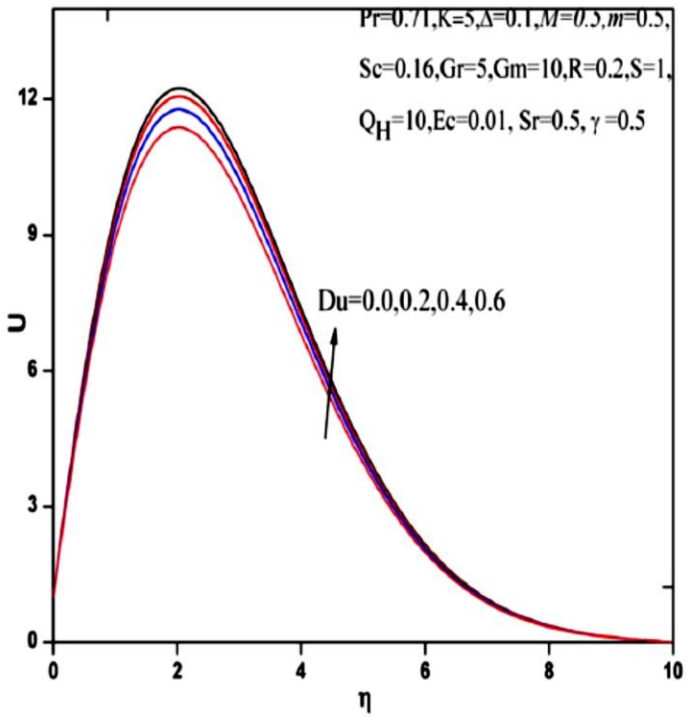

Figure 23: Effect of Dufour number (*Du*) on velocity.

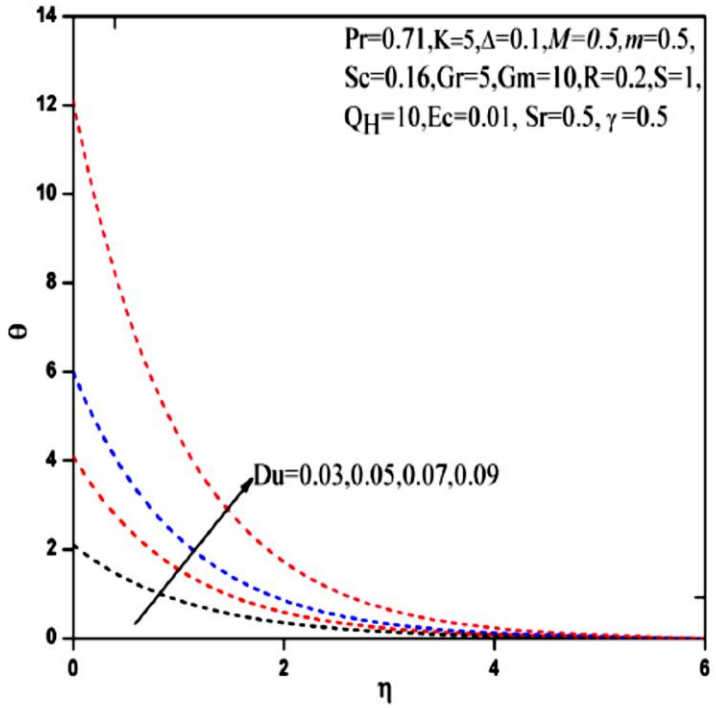

Figure 24: Effect of Dufour number (*Du*) on temperature.

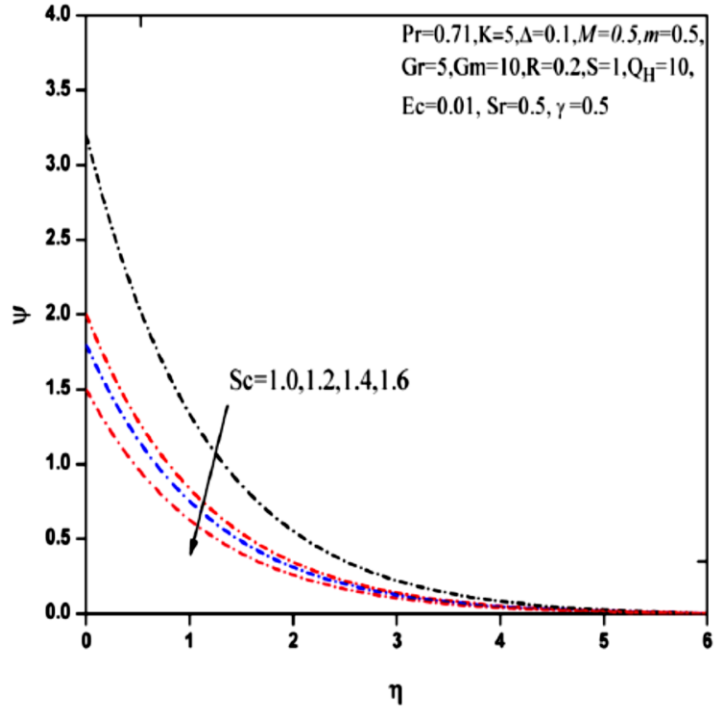

Figure 25: Effect of Schmidt number (*Sc*) on concentration.

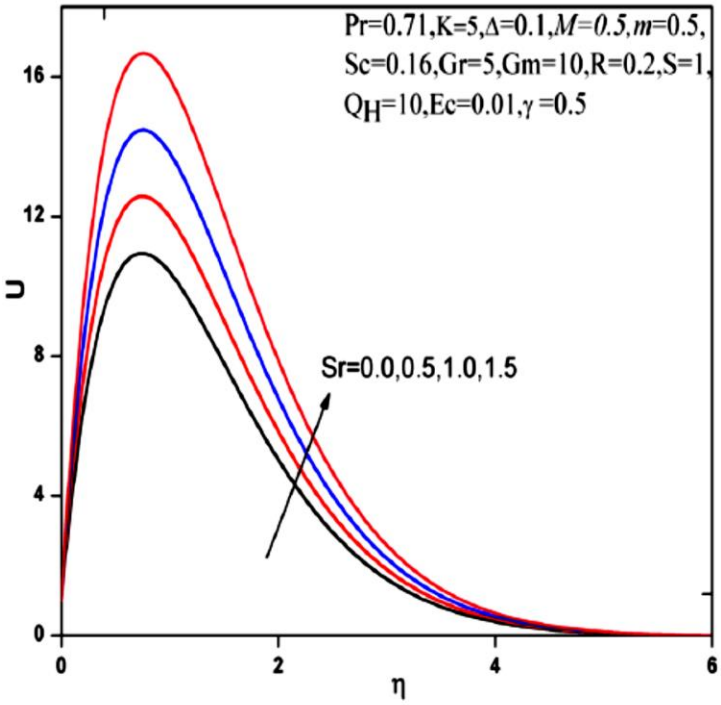

Figure 26: Effect of Soret number (*Sr*) on velocity.

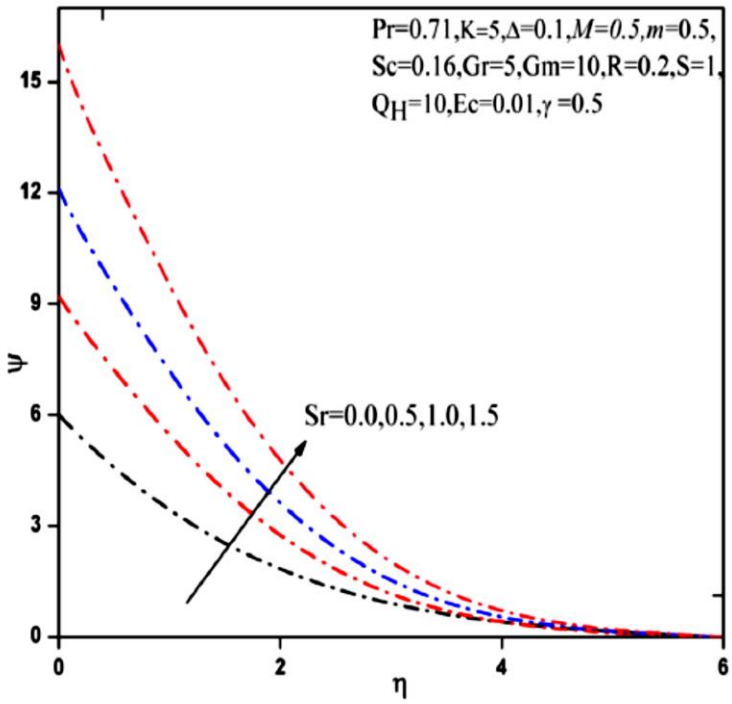

Figure 27: Effect of Soret number (*Sr*) on concentration.

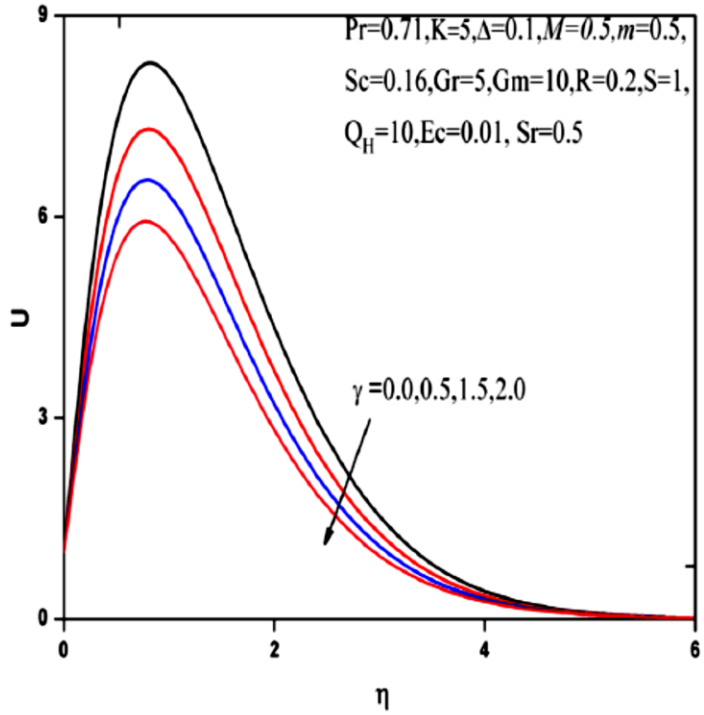

Figure 28: Effect of chemical reaction number (γ) on velocity.

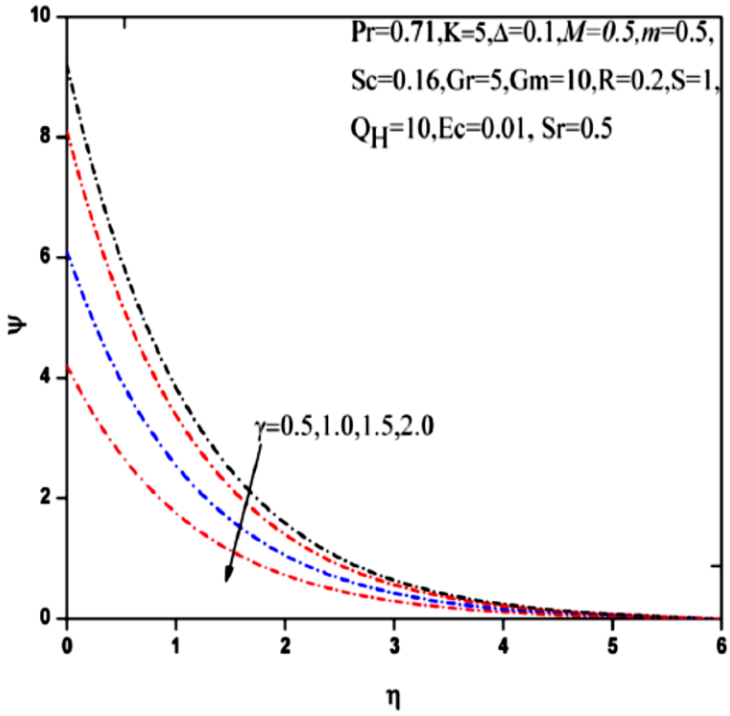

Figure 29: Effect of chemical reaction number (γ) on concentration.

Figure Captions

Figure .1: Flow configuration and coordinate system
Fig. 2: Effect of magnetic body force parameter (M) on velocity.
Figure 3: Effect of magnetic body force parameter (M) on angular velocity (micro-rotation).
Figure 4: Effect of Eringen vortex viscosity parameter (Δ) on velocity.
Figure 5: Effect of Eringen vortex viscosity parameter (Δ) on micro-rotation.
Figure 6: Effect of Hall parameter (m) on velocity.
Figure 7: Effect of Hall parameter (m) on angular velocity (micro-rotation).
Figure 8: Effect of wall suction parameter (S) on velocity.
Figure 9: Effect of wall suction parameter (S) on angular velocity (micro-rotation).
Figure 10: Effect of wall suction parameter (S) on temperature.
Figure 11: Effect of wall suction parameter (S) on species concentration.
Figure 12: Effect of permeability parameter (K) on velocity.
Figure 12: Effect of permeability parameter (K) on velocity.
Figure 13: Effect of permeability parameter (K) on micro-rotation.
Figure 14: Effect of thermal Grashof number (Gr) on velocity.
Figure 15: Effect of species (solutal) Grashof number (Gm) on velocity.
Figure 16: Effect of Prandtl number (Pr) on temperature.
Figure 17: Effect of radiation parameter (F) on velocity.
Figure 18: Effect of radiation parameter (F) on temperature.
Figure 19: Effect of heat absorption parameter (Q_H) on velocity.
Figure 20: Effect of heat absorption parameter (Q_H) on temperature.

Figure 21: Effect of Eckert number (*Ec*) on velocity.
Figure 22: Effect of Eckert number (*Ec*) on temperature.
Figure 23: Effect of Dufour number (*Du*) on velocity.
Figure 24: Effect of Dufour number (*Du*) on temperature.
Figure 25: Effect of Schmidt number (*Sc*) on concentration.
Figure 26: Effect of Soret number (*Sr*) on velocity.
Figure 27: Effect of Soret number (*Sr*) on concentration.
Figure 28: Effect of chemical reaction number (γ) on velocity.
Figure 29: Effect of chemical reaction number (γ) on concentration.

TABLES

Table 1: Comparison of C_f, $-C_w$, Nu/Re_x and Sh/Re_x

	Kundu *et al.* [24]				Present results			
S	C_f	$-C_w$	Nu/Re_x	Sh/Re_x	C_f	$-C_w$	Nu/Re_x	Sh/Re_x
4.0	15.8370	2.73432	1.7040	0.4267	15.837004	2.734323	1.704011	0.426702
5.0	8.65130	1.52070	2.1300	0.5333	8.651306	1.520705	2.130014	0.533307
6.0	3.76030	0.92140	2.55697	0.6400	3.760304	0.921407	2.556974	0.640011

Table 2: Effects of Δ, S, R, Q, Du, F, Sr, and γ on C_f, $-C_w$, Nu/Re_x and Sh/Re_x

Δ	S	R	Q_H	F	Du	Sr	γ	C_f	$-C_w$	Nu	Sh
0.2	2.5	0.2	1.0	0.5	0.5	0.5	1.0	26.7934			
0.4	2.5	0.2	1.0	0.5	0.5	0.5	1.0	27.3257			
0.2	4.0	0.2	1.0	0.5	0.5	0.5	1.0	9.3782	2.1386	1.5873	0.3579
0.2	5.0	0.2	1.0	0.5	0.5	0.5	1.0	5.6423	1.3289	2.3579	0.4936
0.2	2.5	0.5	1.0	0.5	0.5	0.5	1.0	23.4386	12.3295		
0.2	2.5	1.0	1.0	0.5	0.5	0.5	1.0	18.7935	19.5762		
0.2	2.5	0.2	2.0	0.5	0.5	0.5	1.0	20.9746	9.3789	1.3257	
0.2	2.5	0.2	3.0	0.5	0.5	0.5	1.0	14.6358	8.5643	2.5784	
0.2	2.5	0.2	1.0	1.0	0.5	0.5	1.0	32.0589	11.3257	0.6732	
0.2	2.5	0.2	1.0	2.0	0.5	0.5	1.0	45.6842	18.4738	0.4578	
0.2	2.5	0.2	1.0	0.5	1.0	0.5	1.0	36.9738	5.9864	1.2397	
0.2	2.5	0.2	1.0	0.5	1.5	0.5	1.0	44.8376	7.4598	0.9356	
0.2	2.5	0.2	1.0	0.5	0.5	1.0	1.0	37.1589	6.3947		0.1936
0.2	2.5	0.2	1.0	0.5	0.5	2.0	1.0	45.6893	8.5732		0.1725
0.2	2.5	0.2	1.0	0.5	0.5	0.5	1.5	28.9378	2.5738		0.1838
0.2	2.5	0.2	1.0	0.5	0.5	0.5	2.0	27.1387	1.7389		0.2936